UNIVERSITY OF CALIFORNIA

UNIVERSITY OF CALIFORNIA SANTA CRUZ

EXTREMELY CORRELATED FERMI LIQUID (ECFL) DESCRIPTION OF LOW ENERGY EXCITATION SPECTRUM OF HIGH TC CUPRATE SUPERCONDUCTORS MEASURED BY ANGLE RESOLVED PHOTOEMISSION SPECTROSCOPY (ARPES).

A dissertation submitted in partial satisfaction of the
requirements for the degree of

DOCTOR OF PHILOSOPHY

in

PHYSICS

by

Kazue Matsuyama

December 2016

The Dissertation of Kazue Matsuyama
is approved:

Professor Sriram Shastry, Chair

Professor David P. Belanger

Professor Jairo Velasco Jr.

Dean Tyrus Miller
Vice Provost and Dean of Graduate Studies

Table of Contents

List of Figures

Abstract

Extremely Correlated Fermi Liquid (ECFL) description of low energy excitation spectrum of high Tc cuprate superconductors measured by Angle Resolved Photoemission Spectroscopy (ARPES).

by

Kazue Matsuyama

In this dissertation, we present Extremely Correlated Fermi Liquid (ECFL) description of low energy excitation spectrum of high temperature cuprate superconductors measured by Angle Resolved Photoemission Spectroscopy (ARPES). Focusing on interpretation of the ARPES data, we propose a rigorous approach to understanding the unconventional quasiparticle dynamics in high Tc cuprate superconductors. First, we present ARPES line shapes fitting with the ECFL theory. The ECFL theory is very successful in explaining the ARPES spectral functions of high Tc cuprate superconductors, and it fits the ARPES line shapes as functions of momentum (momentum distribution curves, MDCs) and energy (energy distribution curves, EDCs) for different materials and different temperature with the same intrinsic physical variables along the nodal direction. Although it is not the first to fit both MDCs and EDCs of high Tc cuprate superconductors, the ECFL theory offers unprecedented applicability in fitting the ARPES spectral functions. Second, the ECFL theory provides a robust discussion for the origin of kinks in energy dispersion of strongly correlated material measured by ARPES. A bending anomaly in the energy dispersion of strongly correlated matter, the

universal *low energy kink* in the ARPES spectrum ∼50 - 100 meV, can not be explained within the standard linear band dispersion theory because of significant corrections due to interactions. In our work, we address correlation kinks arising from the momentum dependent Dyson self-energy of the ECFL theory. The calculation is overdetermined, and four independent variables can predict sets of measurable relations in the ARPES experiments. We find that ECFL interpretation of the ARPES kinks is consistent with the available experimental data, and we provide a decisive set of predictions for future high resolution ARPES experiments.

To my family and friends.

Acknowledgments

First of all, I would like to thank my dissertation committee members, thank you Professor Sriram Shastry, Professor David Belanger, and Professor Jairo Velasco for agreeing to serve on my dissertation committee and taking time to read my dissertation work from your busy schedule. I would like to express my deepest gratitude to my advisor and chairman in my committee Professor Sriram Shastry for his continuous support, encouragement and patience for me during my Ph.D studies at UCSC. Physics discussion with Dr. Shastry has always been genuinely inspiring. Dr. Shastry has always encouraged me to think *big*, not *small*. I would like to express my sincere thanks to Dr. Gey-Hong Gweon who provided me an opportunity to work at the SSRL beamline. I would like to thank him for sharing his expertise in the ARPES experiment and a great deal of his mentoring support. I would like to sincerely thank Professor Belanger for his support and concern during my graduate studies at UCSC and kindly serving on my committee. Also, I would like to thank Dr. Edward Perepelitsky for stimulating discussion and his insightful comments regarding my work. I appreciate his friendship and support during my graduate studies in Santa Cruz. I also would like to thank people in physics office at UCSC, Davina Walker, Sissy Madden, Maria Sliwinski, and David Sugg for providing me administrative help and support. Thank you all for being friendly and helpful for me. Also, I am deeply grateful to Physics Department at University of California Santa Cruz for providing me an opportunity to study in the US as I'm proud of myself for earning my Ph.D degree from UCSC.

Last, but not the least, I would like to thank my parents, Nobuyo Matsuyama and Yoshimitsu Matsuyama, and my sister Miyuki Mukai and my brother Kouichirou Matsuyama for supporting me and my life.

Chapter 1

Introduction

Angle resolved photoemission spectroscopy (ARPES) is a powerful experimental probe that enables direct measurement of the single-particle excitation spectrum. The unique surface sensitive probe allows us to perform direct observation of the two dimensional surface state to unprecedented levels, and such detailed information is useful to study physics at microscopic length scale. The experiment becomes specially vital when we study surface physics and quasi-low dimensional systems, for example, high Tc cuprate superconductors that the interaction between the layers of which is usually weak. As ARPES offers us rich information about quasiparticle dynamics in a solid, such as direct observation of the electronic band structure and configuration of a Fermi surface, quantitative analysis and interpretation of photoemission data in the ARPES experiments require considerable understanding of many body physics.

In this dissertation, we propose a novel interpretation of the ARPES photoemission data. The new approach to interpreting the ARPES photoemission data has

been constructed based on the theoretical proposal of "Extremely Correlated Fermi Liquid Theory" (ECFL) by Sriram Shastry [1]. The single-particle Green's function of ECFL theory is the solution to the Gutzwiller projected ground state of t-J Hamiltonian. Taking $U \to \infty$ limit in the Hubbard model, we obtain t-J Hamiltonian, and it has been claimed that the t-J model explains the essential physical properties of high Tc cuprate superconductors.

Our goal is to understand the ARPES photoemission data and study quasiparticle dynamics in the cuprate superconductors using ECFL theory. Originally, the theory was introduced to explain the strange metal phase in the phase diagram of the hole doped cuprate superconductors. The first ARPES line shape fitting was conducted for the normal state ARPES data of cuprate superconductors [2]. In this work, line shape fitting with the single particle spectral function of the ECFL theory demonstrated unprecedented success with only two free parameters. It was shown that the ECFL fitting model fits both laser and synchrotron ARPES data of optimally doped $Bi_2Sr_2CaCu_2O_{8+\delta}$ and synchrotron ARPES data of optimally doped $La_{2-x}Sr_xCuO_4$ along the nodal direction. The unprecedented success of ECFL fits is attributed to the key theoretical idea of correlation physics, "caparison factor", and it was shown that the caparison factor plays a central role to fit the line shapes of high Tc cuprate superconductors measured by ARPES.

Second, we have proposed the phenomenological ECFL fitting models and obtained high quality fits for the ARPES line shapes of high Tc cuprate superconductors in Ref. ([3]). In this work, the phenomenological ECFL models have been proposed to

challenge fitting the ARPES spectral functions of cuprate superconductors as functions of momentum (momentum distribution curves, MDCs) and energy (energy distribution curves, EDCs). The momentum distribution curves, MDCs, are given by recording the photo-electron counts as a function of momentum at a fixed energy, and the energy distribution curves, EDCs, are given by recording the photo-electron counts as a function of energy at a fixed momentum. We constructed the phenomenological ECFL models by scrutinizing the behavior of the caparison factor that is an "ω dependent adaptive spectral weight" that imposes correlation physics of ECFL and Gutzwiller projection. Gutzwiller projection of ECFL theory works to decrease the spectral weight at high energy, but it simultaneously holds the Fermi surface volume invariance at low energy. In this work, it was demonstrated that the proposed phenomenological ECFL models successfully fit both EDCs and MDCs of ARPES spectral functions of the two different optimally doped cuprate superconductors $Bi_2Sr_2CaCu_2O_{8+\delta}$ and $La_{2-x}Sr_xCuO_4$ with the identical intrinsic fitting variables along the nodal direction. However, we should note that our model was not the first to fit both MDCs and EDCs line shapes of cuprate superconductors, the unprecedented applicability of the model in fitting the ARPES spectral functions of cuprates was an achievement.

Finally, the ECFL theory provides a rigorous discussion for the origin of kinks in the low energy ARPES spectra of strongly correlated materials. The bending anomaly in energy dispersion of strongly correlated matter has been well known in the ARPES community, and in past, several theoretical proposals invoking local Bosonic excitations were considered to discuss its origin, yet none of these proposals was rigorously conclu-

sive. Therefore, no consensus concerning the origin of kinks in the ARPES spectra has been established.

The low energy kink in the ARPES spectra of strongly correlated materials is a bending anomaly in energy dispersion around binding energy of ∼50 - 100 meV. Because the standard linear band theory can not reproduce it, its origin should be ascribed to corrections due to interactions. Low energy kinks in the ARPES spectra have been observed in cuprate superconductors, and in other strongly correlated materials, such as charge density wave systems, cobaltates, and ferromagnetic iron surfaces. Kinks have been observed below and above Tc, at wide momentum range from nodal to anti-nodal direction, and over the entire doping range from insulator to normal metal in the hole doped phase diagram of cuprates. While past reports often focus on reporting kinks in MDCs dispersion, we address the significance of investigating kinks in EDCs dispersion as well. First, we propose an effective protocol for extracting the kink momentum and energy from the ARPES data. Second, we demonstrate that the available ARPES data is consistent with the correlation description of kinks, and we show that strong correlations give rise to the kinks in the low energy ARPES spectra in the most robust manner. Last, our investigation suggests a decisive set of predictions for future high quality experiments.

In short, this dissertation focuses on analysis and interpretation of the ARPES data of strongly correlated materials. First, I discuss the ARPES line shape fitting with the ECFL theory. Second, I present the correlation explanation for the origin of low energy kinks in the ARPES spectra. There will be summary and concluding remarks

and some more results of ECFL theory in the end.

1.1 A brief introduction to ARPES photoemission theory: Sudden Approximation

In this section, I present a short summary of ARPES theory that one should know in order to understand our work in this dissertation. The short outline here focuses on explaining the theoretical approach of sudden approximation in photoemission experiments, and the outline should show that the sudden approximation directly relates the measured ARPES spectrum and the single-particle Green's function [4, 5].

The whole idea of ARPES photoemission experiments is based on the photoelectric effect that says an electron escapes from solid surface as a result of quantum mechanical interaction between the incident photon and electrons in the solid. The ARPES experiments measure the kinetic energy of escaped "photoelectrons" and record the photo-electron counts as a function of energy and momentum. The measured kinetic energy of the photoelectron maps out the electronic band structure of the sample as functions of momenta parallel to the sample surface. When measuring the kinetic energy of the photoelectrons, we assume the sudden approximation that says the photoemission process happens instantaneously. This is equivalent to saying, for example, for an interacting N electron system, we assume that the final state of N-1 electron system does not interact with the emitted photoelectron. The assumption should be valid when the kinetic energy of the photoelectron is large, but can be inappropriate when the kinetic

energy of the photoelectron is small. Break down of the sudden approximation of the low photon energy experiment can be interesting topic to discuss, but it is beyond the scope of this dissertation.

To illustrate the sudden approximation in the photoemission process mathematically, we write the interaction Hamiltonian for photons interacting with electrons in the sample,

$$H_{int} = \frac{q_e}{2\,m_e}(\mathbf{p}\cdot\mathbf{A} + \mathbf{A}\cdot\mathbf{p}) \tag{1.1}$$

to simplify our calculation, we let c = $\hbar$ = 1. q_e is the electron charge, m_e is the electron mass, $\mathbf{A}$ is the vector potential of the photon field, and $\mathbf{p}$ is the momentum of an electron. Next, quantizing the vector potential of the photon field, the second quantization representation for this interaction Hamiltonian becomes

$$H_{\rm int} = \sum_{\mathbf{k_p},\mu} \frac{q_e}{m_e}\frac{1}{\sqrt{V\,\omega_p}}\exp(i\mathbf{k}_p\cdot\mathbf{x} - i\omega_p t)\hat{\epsilon}_\mu\cdot\mathbf{p}\alpha_{\mu,\mathbf{k_p}} + h.c., \tag{1.2}$$

where, in the finite volume V, $\alpha_{\mu,\mathbf{k_p}}$ is the annihilation operator for a photon with polarization vector $\hat{\epsilon}_\mu$, and $\mathbf{k_p}$ and ω_p are the momentum and energy of a photon.

This interaction Hamiltonian indicates the excitation of electrons from the initial state Ψ_i to the final state Ψ_f by the vector potential of the photon field leads to the emission of photoelectrons. When we write the initial and final state wavefunctions

to describe the photoemission process, we consider the one electron approximation. For the N electron system, we assume that the initial wavefunction is written as a product of the orbital wavefunction, ϕ_k, where emission of an electron by photoexcitation takes place, and the remaining initial N-1 electron wavefunction, $\psi^k_{i,N-1}$. The initial state wavefunction then becomes $\Psi_i = \mathrm{c}\,\phi_{i,k}\psi^k_{i,N-1}$, and the operator c here antisymmetrizes the wavefunction. Similarly, the final state wavefunction is also written as a product of the wavefunction of the photoelectron ϕ_{f,E_k} and the remaining final N-1 electron wavefunction, $\psi^k_{f,N-1}$. Therefore, the final state wavefunction becomes $\Psi_f = \mathrm{c}\,\phi_{f,E_k}\psi^k_{f,N-1}$. For these initial and final state wavefunctios, we write the photocurrent expression that is proportional to the transition probability of the photoemission process. Using the Fermi's Golden rule,

$$\mathrm{I}(\mathbf{k},\mathrm{E}) = 2\pi \sum_{f,i,\mathbf{k}} |\,\langle \Psi_f \,|\, H_{\mathrm{int}} \,|\, \Psi_i \rangle|^2\, \delta(\mathrm{E}_f - \mathrm{E}_i - \hbar\omega_p) \tag{1.3}$$

writing down this in terms of the initial and final state wavefunction,

$$\mathrm{I}(\mathbf{k},\mathrm{E}) = 2\pi \sum_{f,i,\mathbf{k}} |\,\langle \phi_{f,E_k} \,|\, H_{\mathrm{int}} \,|\, \phi_{i,k} \rangle \sum_l \langle \psi^k_{l,N-1} \,|\, \psi^k_{i,N-1} \rangle\,|^2\, \delta(\mathrm{E}_f + \mathrm{E}_{l,\text{N-1}} - \mathrm{E}_i - \hbar\omega_p) \tag{1.4}$$

Note that when rewriting the photocurrent in terms of the initial and final state wavefunctions, we introduce the running subscript l for the final N-1 electron

wavefunction, $\psi^k_{f,N-1}$, changing from f to l. This is because we include the probability of exciting the N-1 electron system after removing an electron from the orbital wavefunction, ϕ_k, of the initial N electron system. Here, the running subscript l denotes the number of l excited states of the N - 1 electron system. We consider that there are l excited states for the final N - 1 electron system with wavefunctions $\psi^k_{l,N-1}$ at energy of $\mathrm{E}_{l,\mathrm{N\text{-}1}}$. Considering of excitation of N - 1 electron system is necessary and becomes significant when we describe interacting system. Intuitively, we should imagine that the final system after emitting an electron tries to accommodate the change in the electron distribution and redistribute remaining N-1 charges, so the system successfully minimizes its energy.

The mathematical expression of photocurrent with wavefunction $\psi^k_{l,N-1}$ in Eq. (1.4) is useful to illustrate distinct pictures of ARPES spectrum with and without electron interactions in a solid. For example, consider the non interacting system, the overlap integral of N-1 electrons becomes 1 for specific l, and the ARPES spectrum should plot a delta function at $l = \mathrm{k}$, for that single orbital k. On the contrary, considering of the interacting system, we see the spectrum that is different from the one for the non interacting system. The ARPES spectrum of the interacting system is different from that of the non interacting system because the strong correlation leads to overlapping between states of N - 1 electron system. The photoexcitation at the specific orbital k produces the number of excited states l for that orbital k, and the ARPES spectrum should plot the main delta function and additional lines of interacting states for $l \neq \mathrm{k}$.

Finally, many body physics let us write down the photocurrent in Eq. (1.4) proportional to the spectral function [6], A($\mathbf{k}$, E),

$$\mathrm{I}(\mathbf{k},\mathrm{E}) \propto \sum_{f,i,\mathbf{k}} |\, \langle \phi_{f,E_k} \,|\, H_{\mathrm{int}} \,|\, \phi_{i,k} \rangle \,|^2 \, f\,(\mathrm{E}-\mu)\, \mathrm{A}(\mathbf{k},\mathrm{E}) \tag{1.5}$$

Here, A($\mathbf{k}$, E) is the spectral function that is the imaginary part of the single particle Green's function, A($\mathbf{k}$, E) = π^{-1}ImG($\mathbf{k}$, E). This mathematical expression says the spectral function determines the probability of removing or adding an electron at momentum $\mathbf{k}$ and energy E. The Fermi-Dirac function, $f(\mathrm{E}-\mu)$, specifies the probability of removing an electron from the occupied states. The one electron matrix element gives the probability of photoexciting the removed electron to the higher energy photoelectron state. We should note that the mathematical expression in Eq. (1.5) describes that the sudden approximation separates the two photoemission steps, removing an electron and exciting the removed electron to the higher energy photoelectron state. Consequently, understanding the ARPES spectrum of strongly correlated materials requires the knowledge of the spectral function of strongly correlated materials.

Incidentally, the ECFL theory provides us such spectral function for strongly correlated materials. In the following chapters, I discuss the spectral function of the ECFL theory and its interpretation of the ARPES spectra of strongly correlated materials.

Chapter 2

Phenomenological model for the normal state ARPES line shapes of high temperature superconductors

This chapter reproduces the published material, Matsuyama, K, and Gweon, G-H. "Phenomenological Model for the Normal-State Angle-Resolved Photoemission Spectroscopy Line Shapes of High-Temperature Superconductors". *Physical Review letters* **111**.24 (2013): 246401. Here, we would like to mention the new report on the ARPES line shapes. In past, the ARPES experiments was reporting the strong asymmetric EDCs line shapes (energy distribution curves, ARPES intensity measurement as a function of energy at a fixed momentum) and the very symmetric MDCs line shapes (momentum distribution curves, MDCs, ARPES intensity measurement as a function of momentum at a fixed energy). However, the most recent ARPES experiment has reported asymmetric MDCs line shapes near the Fermi level for some of cuprates

superconductors, for example Hg1201 in Ref. ([58]). We suggest possibly intrinsic asymmetry in the MDCs line shapes near the Fermi level, but investigation of it should require high resolution ARPES experiments.

2.1 Abstract

Providing a full theoretical description of the single particle spectral function observed for high temperature superconductors in the normal state is an important goal, yet unrealized. Here, we present a phenomenological model approaching towards this goal. The model results from implementing key phenomenological improvement in the so-called extremely correlated Fermi liquid (ECFL) model. The model successfully describes the ARPES spectral function as functions of momentum and energy and fits data for different materials ($Bi_2Sr_2CaCu_2O_{8+\delta}$ and $La_{2-x}Sr_xCuO_4$), with an identical set of intrinsic parameters. The current analysis goes well beyond the prevalent analysis of the spectral function as a function of momentum alone.

2.2 Introduction

In the sudden approximation theory [5] of the angle resolved photo-electron spectroscopy (ARPES), photo-electron counts, $I(\vec{k}, \omega)$, recorded as a function of mo-

mentum ($\vec{k}$) and energy (ω) [1] are given by

$$I(\vec{k},\omega) = |M_{if}|^2 \, f(\omega) \, A(\vec{k},\omega) \tag{2.1}$$

where M_{if} is the dipole matrix element for the photo-excitation, $f(\omega)$ is the Fermi-Dirac function, and $A(\vec{k},\omega) = \frac{1}{\pi}\mathrm{Im}\, G(\vec{k},\omega)$ is the single particle spectral function, where G is the single particle Green's function [2].

As the single particle Green's function in the normal state is believed to contain vital information on the nature of excitations relevant to the high temperature ("high T_c") superconductivity, its characterization by ARPES has been a major line of research. Various approaches towards getting at this information have been attempted: a phenomenological approach based on a simple scaling behavior of the electron self energy [7], an asymptotic solution to the Gutzwiller projected ground state of the t-J Hamiltonian [8], application of a non-Fermi liquid theory [9] for low dimensions, and a newly proposed solution to the t-J Hamiltonian [1].

For an experimental "cut," i.e. an experimental data set taken along a line of $\vec{k}$ values, $I(\vec{k},\omega)$ is a function defined on a two dimensional domain. This multi-dimensionality makes analyzing $I(\vec{k},\omega)$ a non-trivial task. While attempts [10] have been made to analyze the $I(\vec{k},\omega)$ image (e.g., see Fig. 2.5(a)) as a whole, the current understanding of line shapes in terms of $A(\vec{k},\omega)$ depends on the analysis of selected energy distribution curves (EDCs; the EDC is a function of ω, defined as $I(\vec{k}=\vec{k}_0,\omega)$)

[1] We use $\hbar = 1$ by convention.
[2] We use the advanced Green's function.

[2, 7, 8, 12] or selected momentum distribution curves (MDCs; the MDC is a function of $\vec{k}$, defined as $I(\vec{k}, \omega = \omega_0)$, with $\vec{k}$ varying along a line) [12, 13].

Currently, there is no consensus on a theoretical model that can suitably describe ARPES data of high T_c materials. A model that can describe the normal state data, both EDCs and MDCs, obtained in different experimental conditions and for different materials, with the same intrinsic parameters would be a good candidate. Here, we propose a new such phenomenological model.

The new theory, so-called Extremely Correlated Fermi liquid (ECFL)[1] arises, and it was shown to be quite successful in describing EDCs [2]. The new model now makes it possible to describe other key aspects of the data as well: MDC fits are excellent and the values of $|M_{if}|^2$ behave reasonably. And, it improves EDC fits. The result is a phenomenological model in which the apparent dichotomy between the EDCs and the MDCs [9, 14] is described excellently by two independent aspects of a single theoretical concept, the caparison factor [1, 2].

A phenomenological study of this kind seems to be helpful, also in light of the ongoing development of the ECFL theory [15, 16]. The theoretical formalism of ECFL initiated by Shastry [1, 15] is quite involved, and, while a numerical solution [16] valid for hole doping $x \gtrsim 0.3$ is now available, more time seems necessary to extend these promising results to near-optimal doping. Thus, a phenomenological model based on the main feature of the theory, the caparison factor, may be of considerable value at this stage. In this theory [15], the caparison factor is an *ω-dependent adaptive spectral weight* that encodes two key pieces of physics: the Gutzwiller projection that reduces

the spectral weight at high ω and the invariance of the Fermi surface volume at low ω.

In our previous work [2], it has been demonstrated that the normal state EDCs for optimally doped cuprates for two different compounds, or for different experimental conditions (low photon energy or high photon energy), can be explained using an ECFL line shape model, all with one set of intrinsic parameters. We will refer to that ECFL as the "simplified ECFL (sECFL)" [1], in relation to the fuller theory in development [15, 16]. While the EDC analysis used there has strong merits [2, 18], a natural subsequent question is whether MDCs can be described as well, along the same line of theory.

2.3 Introduction to the theoretical models

In the sECFL model [2], $G(\vec{k},\omega)$ is given by

$$G(\vec{k},\omega) = \frac{Q_n - \frac{n^2}{4}\frac{\Phi(\omega)}{\Delta_0}}{\omega - \varepsilon(\vec{k}) - \Phi(\omega)} \tag{2.2}$$

where $Q_n = 1 - \frac{n}{2} = \frac{1+x}{2}$ is the total spectral weight per $\vec{k}$ in the t-J model, and n (x) is the number of electrons (holes) per unit cell [3]. $\Phi(\omega)$ is an ordinary Fermi liquid self energy, determined by two intrinsic parameters, Z_{FL} (quasi-particle weight) and ω_0 (cutoff energy scale), and one extrinsic parameter η (impurity scattering contribution to $\mathrm{Im}\,\Phi$). Δ_0 is an energy scale parameter, determined completely by n, Z_{FL}, and ω_0, through the global particle sum rule.

It is for the probable benefit to us that we now summarize key results of the

[3] We now use the symbol $\varepsilon(\vec{k})$, instead of $\xi(\vec{k})$ in Ref. ([2]), for the one electron energy.

work in Ref. ([2]). The Dyson self energy of the AFL, Φ, is given by (as given by Eq. (2.2) and footnote 6 of Ref. ([2]))

$$\mathrm{Im}\,\Phi(\omega) = \frac{\omega^2+\tau^2}{\Omega_0}\, e^{-\frac{\omega^2+\tau^2}{\omega_0^2}} + \eta, \tag{2.3}$$

$$\Re\Phi(\omega) = \frac{-1}{\sqrt{\pi}\,\Omega_0}\, e^{-\frac{\tau^2}{\omega_0^2}} \left[\omega_0\omega - 2(\omega^2+\tau^2) D\left(\frac{\omega}{\omega_0}\right)\right], \tag{2.4}$$

where $\tau = \pi k_B T$, $Z_{FL} = \left(1+\frac{\omega_0}{\sqrt{\pi}\Omega_0}\right)^{-1}$, and $D(x) = \frac{\sqrt{\pi}}{2} e^{-x^2}\mathrm{erfi}(x)$ is the Dawson function. EDC fits in Ref. ([2]) used fixed values of $Z_{FL} = 1/3$ and $\varepsilon(\vec{k})$. The experimental data that helped fix these values are the ARPES data taken up to very high binding energy [10]. Using such data it was possible to find the quasi-particle dispersion renormalization ratio due to the high energy ARPES "kink," Z_{FL}. It was also possible to fix $\varepsilon(\vec{k})$, by taking it to have the same form as the tight-binding band dispersion well-known in the literature, which was scaled to give the correct bandwidth measured by the ARPES data. This left only two free fit parameters, η and ω_0. Of these two, η is the impurity scattering parameter, which we associated with the effective sample quality probed by the ARPES technique under different conditions; it is determined in practice by the width of the sharpest quasi-particle peak of a given data set, ≈ 0.04 eV for data taken with low energy photons (e.g., from laser) and 3 or 4 times greater for data taken with high energy photons at synchrotrons. Thus, the only intrinsic fit parameter was ω_0, which was determined from fits as $\omega_0 = 0.5 \pm 0.1$ eV. Then, through a theoretical constraint equation, $\Delta_0 = 0.12 \pm 0.02$ eV was determined. Fitting study in Ref. ([2]) was able to successfully interpret ω_0 and Δ_0 as the purely electronic high

and low ARPES kink energy scales, respectively (Fig. 5 of Ref. ([2])). This interpretation provided these two energy scale parameters with their physical meanings. In the current work, we use the values of all of the intrinsic parameters ($Z_{FL}, \omega_0, \Delta_0$) without change from Ref. ([2]), as we found that all fits were stable under small variations of these parameters. However, small variations of $\varepsilon(\vec{k})$ were necessary, as we describe this in 2.3.1.

The above Green's function can be rewritten as

$$G(\vec{k},\omega) = \frac{Q_n}{\gamma_n} + \frac{\mathcal{C}_n(\vec{k},\omega)}{\omega - \varepsilon(\vec{k}) - \Phi(\omega)} \tag{2.5}$$

$$\mathcal{C}_n(\vec{k},\omega) = Q_n \left(1 - \frac{\omega - \varepsilon(\vec{k})}{\gamma_n}\right) \tag{2.6}$$

where $\mathcal{C}_n(\vec{k},\omega)$ is the "caparison factor" [1, 2] and the energy scale Δ_0 is absorbed into $\gamma_n \equiv 4Q_n\Delta_0/n^2$. As all symbols in Eq. 2.5 other than $\Phi(\omega)$ are real,

$$A(\vec{k},\omega) = \mathcal{C}_n(\vec{k},\omega)\, A_{FL}(\vec{k},\omega) \tag{2.7}$$

where A_{FL} is the spectral function for the "auxiliary Fermi liquid (AFL)" Green's function [4], $A_{FL} = \frac{1}{\pi}\,\mathrm{Im}\, G_{FL} = \frac{1}{\pi}\,\mathrm{Im}\,[\omega - \varepsilon(\vec{k}) - \Phi(\omega)]^{-1}$.

The caparison function $\mathcal{C}_n$, summarized concisely in Eq. 2.6, played the central role in the sECFL model. In this work, we show how its role can be extended even further by a key phenomenological modification: *inspired by data, we treat the ω dependence*

[4] As in Ref. [2], subscript "FL" means the AFL (auxiliary Fermi liquid)

and the $\vec{k}$ dependence of $\mathcal{C}_n$ as separately adjustable. We shall refer to the modified model as pECFL, where p stands for "phenomenological." We distinguish between MD-pECFL and MI-pECFL based on whether $\mathcal{C}_n$ remains momentum dependent (MD) or made momentum-independent (MI).

With this much introduction to our models, we shall first discuss line shape fits, before discussing the models. As for free fit parameters controlling the line shape, all models have η and ω_0, like sECFL [2]. In addition, the group velocity, v_{F0}, of $\varepsilon(\vec{k})$, required small adjustment for different models to give correct peak positions as described in next subsection. Then, only for MD-pECFL, there are two more free fit parameters.

2.3.1 One electron dispersion relation

For all fits in this work, $\varepsilon(\vec{k})$ could be approximated as a line, $\varepsilon(\vec{k}) = v_{F0}(k - k_F)$, due to the small energy range and the momentum range involved, as far as $\varepsilon(\vec{k})$ is concerned. We found that the model-dependent variation on v_{F0} was required in order for the fits to describe experimental peak positions correctly. For fitting the Bi2212 data, $v_{F0} = 5.5$ (sECFL) and 6.3 eVÅ (MD-pECFL, MI-pECFL). In panel (a) in Fig. 2.5, $\varepsilon(\vec{k})$ values for pECFL fits are shown. For fitting the LSCO data in Fig. 2.8, $v_{F0} =$ 4 (sECFL), 5 (MD-pECFL), and 5.5 eVÅ (MI-pECFL) were used. This variation in v_{F0} is consistent with the amount of uncertainty in knowing the precise band width (Ref. [10]); it implies small additional uncertainties for the intrinsic parameters Z_{FL}, ω_0, and Δ_0.

2.4 ARPES line shape fits of Bi2212 data

2.4.1 Fits of the Bi2212 180 K data

Figure 2.1 shows ARPES line shape fits for the normal state data for the optimally doped $Bi_2Sr_2CaCu_2O_{8+\delta}$ (Bi2212) sample, taken along the "nodal direction," $(0,0) \rightarrow (\pi,\pi)$. Panel (a) shows fits essentially identical with those in Ref. [2]. The slight difference is due to a slight change of η ($0.17 \rightarrow 0.18$ eV), noted in the caption of Fig. 2.1. The fit quality of MI-pECFL is clearly the best, while that of MD-pECFL is noticeably poorer, despite more fit parameters.

Figure 2.2 shows ARPES line shape fits for MDCs of the same data set. Panel (a) shows clearly that the sECFL has difficulty fitting the data even at $\omega = 0$ (Fermi energy). Panel (b) shows a quite improved fit by the MD-pECFL model. However, the MI-pECFL fit shown in panel (c) is definitively the best.

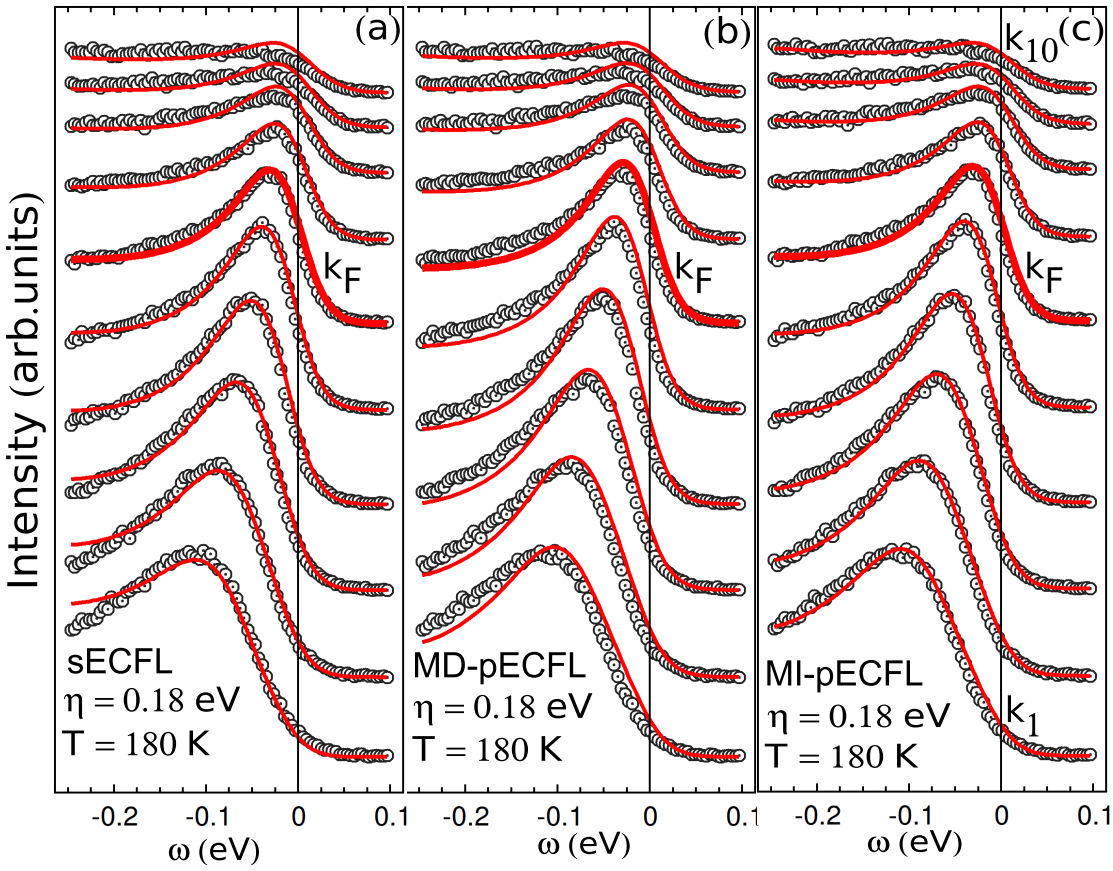

Figure 2.1: Line shape fits of EDCs for Bi2212 ($x = 0.15$) measured at 180K using (a) sECFL, (b) MD-pECFL, and (c) MI-pECFL. Data and model parameters are identical with those in Ref. [2] ($Z_{FL} = 0.33$, $\omega_0 = 0.5$ eV, $\Delta_0 = 0.12$ eV), except for slightly different values for η (0.17 $\rightarrow$ 0.18 eV) and $\varepsilon(\vec{k})$ (see text).

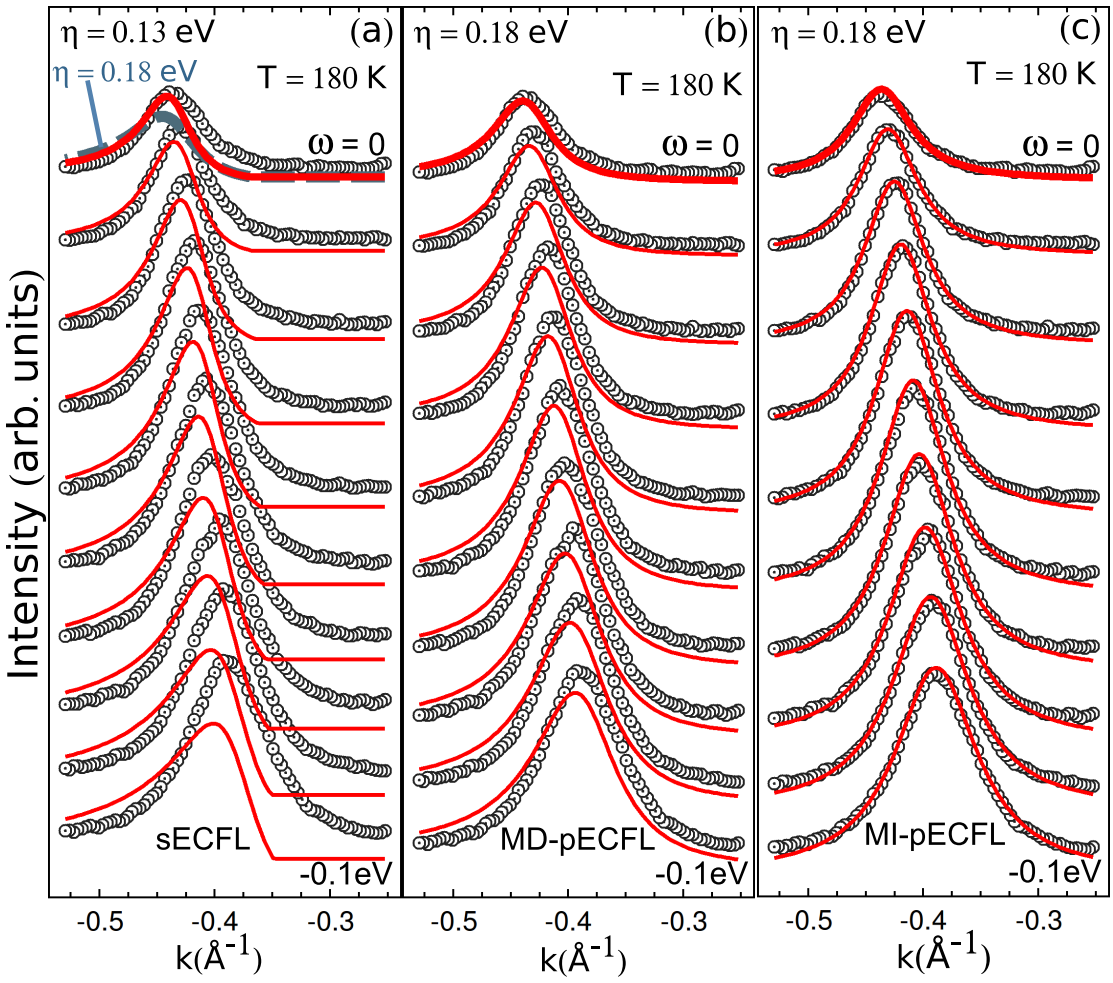

Figure 2.2: Line shape fits of MDCs for Bi2212 ($x = 0.15$) measured at 180 K using (a) sECFL and (b) MD-pECFL and (c) MI-pECFL. Fit parameters are identical with those used for Fig. 2.1, except for the reduced η value (0.13 eV) for (a).

That the MI-pECFL model is able to describe EDCs and MDCs so accurately. In these fits, no extra component (e.g., extrinsic background intensity) was added to the theory that we described thus far. A small "elastic background line shape" (0.5 times the raw line shape for $k \gg k_F$) had been subtracted prior to fit, as explained in Ref. [2]. All of the conclusions above also apply to the fits of the 91 K data [2] as well.

2.4.2 Fits of the Bi2212 91 K data

Here, we show that the ARPES data at 91 K, right at T_c, of this material, is described equally well by the MI-pECFL model. Fig. 2.3 shows that the MI-pECFL model describes the EDCs the best, while the other two models are still quite good. Fig. 2.4 shows that the MI-pECFL model describes the MDCs the best, while the other two models come significantly short. In particular, the sECFL model does very poorly, even when the η parameter is reduced, against the principle that both EDCs and MDCs must be described by the same set of parameters (cf. Fig. 2.3), just to help the fit, as shown in panel (a).

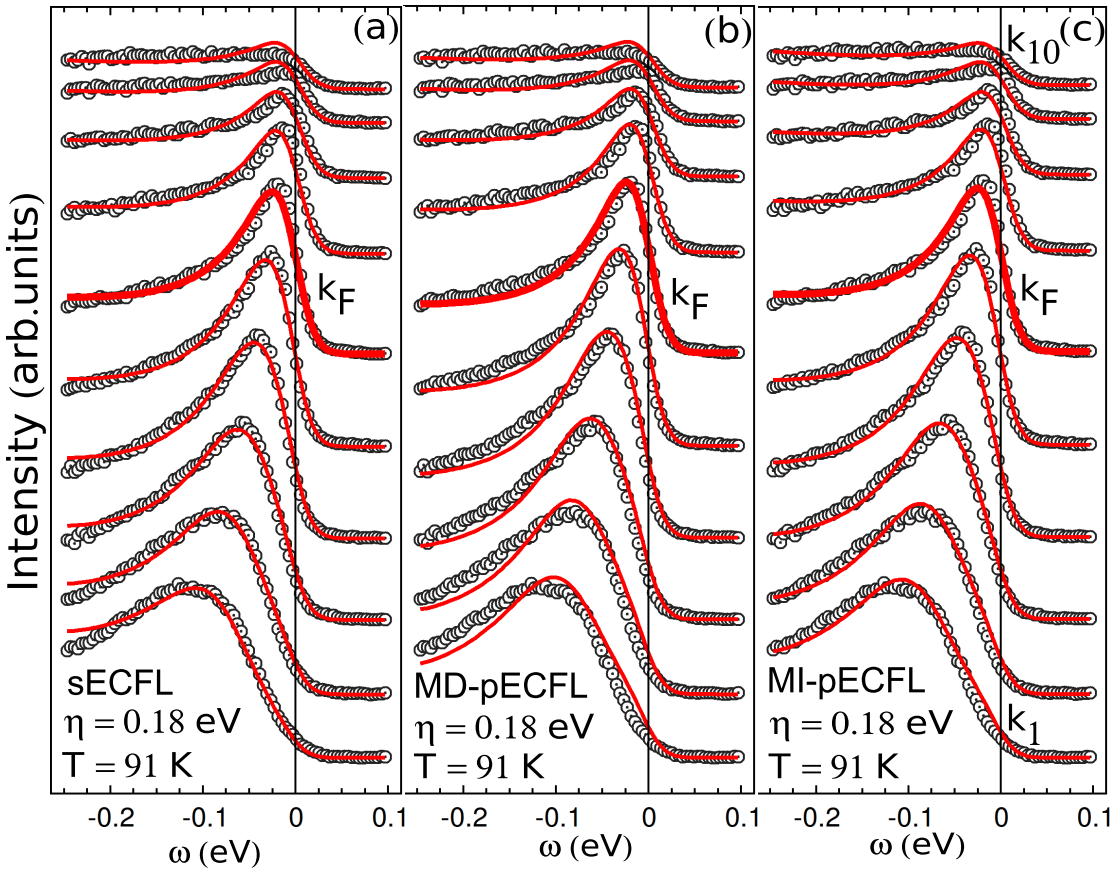

Figure 2.3: Line shape fits of EDCs for Bi2212 ($x = 0.15$) measured at 91 K using (a) sECFL, (b) MD-pECFL, and (c) MI-pECFL. Except the temperature and the overall intensity scale (see Fig. 2.6), all parameter values used for the fit are the same as those used for the 180 K data.

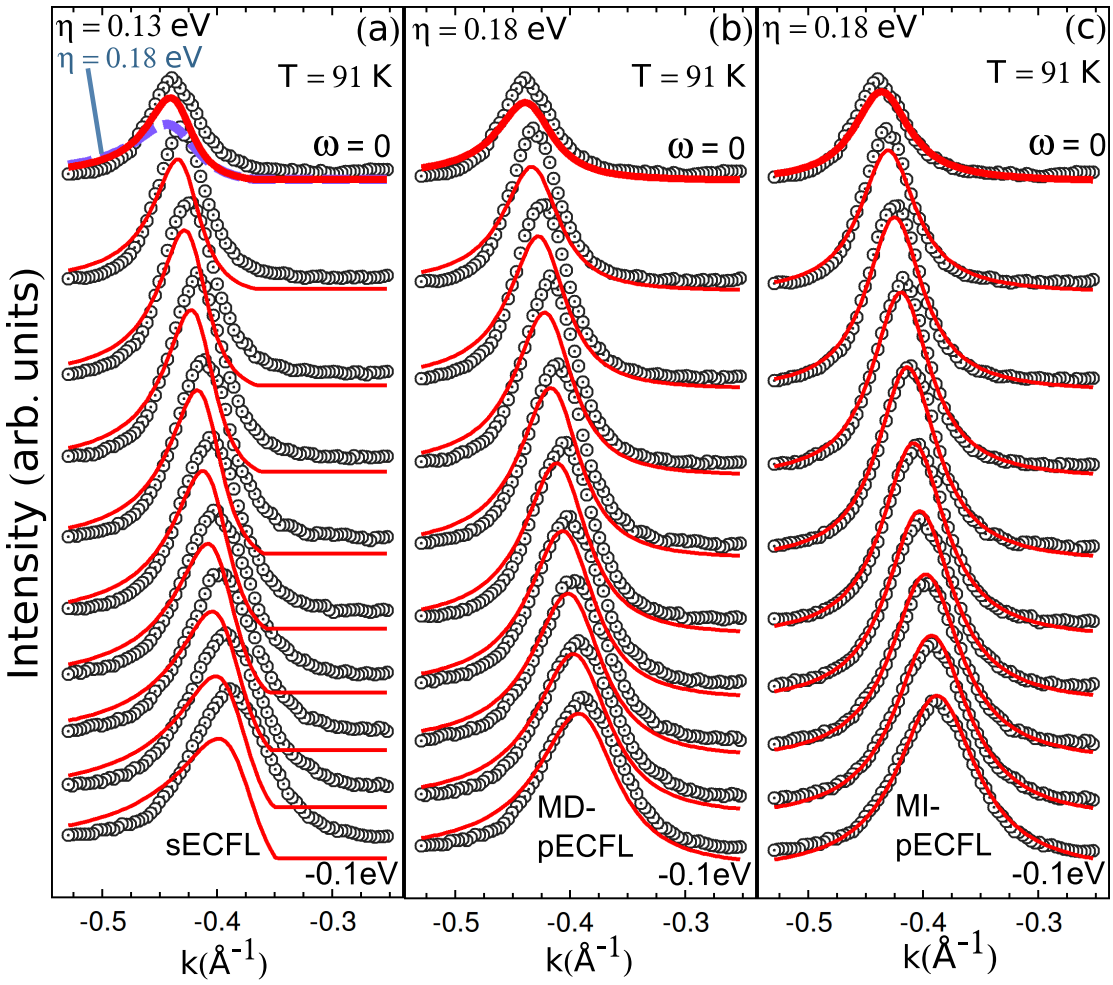

Figure 2.4: Line shape fits of MDCs for Bi2212 ($x = 0.15$) measured at 91 K, using (a) sECFL and (b) MD-pECFL and (c) MI-pECFL. Except the temperature and the overall intensity scale (see Fig. 2.6), all parameter values used for the fit are the same as those used for the 180 K data.

2.4.3 Analysis of fitting results

From the above work, it is clear that the MI-pECFL model emerges as the best model for the Bi2212 data. This model is surprisingly simple: the $\varepsilon(\vec{k})$ term in Eq. 2.6 is simply dropped. The motivation for doing so is purely empirical: the MDCs

of Bi2212 data are known to be quite symmetric and Lorentzian-like. The effect of this simple modification is surprisingly very good in many ways. Without any additional fit parameter, MDC fits improve dramatically, as expected (Fig. 2.2(c)), but EDC fits improve also (Fig. 2.1(c)), especially for $\vec{k}$ far away from $\vec{k}_F$ (Fig. 2.5(b)). Furthermore, the overall scale parameters for MDC fits (Fig. 2.5(c)) and EDC fits (Fig. 2.5(d)) are now quite reasonable, as discussed in the caption.

91 K fit results are in complete agreement with these findings in 180 K fit results, and these facts lend an overwhelming support to the MI-pECFL model. Fig. 2.6 shows the 91 K data as an image, and also shows the overall scale factors, $|M|^2 f(\omega)$ as a function of ω and $|M|^2$ as a function of $\vec{k}$, as extracted from MDC fits and EDC fits, respectively. In great agreement with Fig. 2.5, we see that the MI-pECFL model implies the most reasonable trend for the matrix element.

However, note that 91 K is the transition temperature of optimally doped Bi2212. As the ECFL theory is the theory of the normal state, there is a reason to doubt or question the applicability of the model at very low energies at this temperature. For instance, the rather noticeable discrepancy between the theory MDC and the measured MDC at $\omega = 0$, as can be noticed in Fig. 2.4(c), may be related to the inadequate nature of the theory at low energies for temperatures close to, or below, the superconducting transition temperature. We discuss related issues in more detail in section (2.5.1).

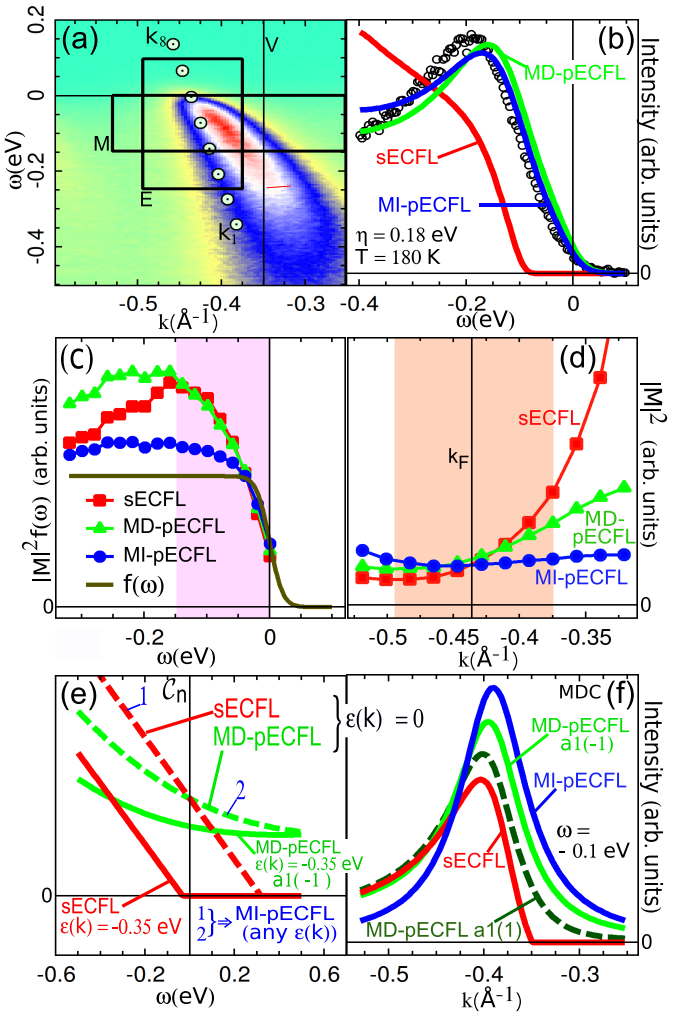

Figure 2.5: (a) The ARPES data for Bi2212 at 180 K, fit in Fig. (2.1) and Fig. (2.2). Rectangle E (M) marks the range of data fit in Fig. 2.1 (2.2). Circle symbols mark $\varepsilon(\vec{k})$ values used in the pECFL fits. ARPES count increases from green, blue (half max), white, to red (max). (b) EDC and its fits, for $\vec{k}$ value marked by the vertical line V in (a). (c,d) The overall intensity scale parameters determined from the MDC fit (c) and the EDC fit (d), which correspond to $|M|^2 f(\omega)$ and $|M|^2$, respectively, by Eq. 2.1. Shaded areas marks the fit ranges used in Figs. 2.1 and 2.2. As the energy dependence of $|M|^2$ is expected to be weak for this small range of ω, we expect the points shown in panel c to approximately follow $f(\omega)$ (line). MI-pECFL does this the best. We also expect points in (d) to show only a modest variation in this k range [10, 11]. Here also, MI-pECFL performs the best; in contrast, sECFL shows an unnatural steep increase. (e) $\mathcal{C}_n(\vec{k},\omega)$ for various models used. For MD-pECFL, $a_1 = -1$ and $a_2 = 2$ are used throughout this Letter. For sECFL, $\max(\mathcal{C}_n(\vec{k},\omega), 0)$ is used [2]. (f) The evolution of the MDC asymmetry, controlled by a_1 within MD-pECFL ($a_2 = 2$). The MDC by sECFL is the most asymmetric, while that by MI-pECFL is completely symmetric.

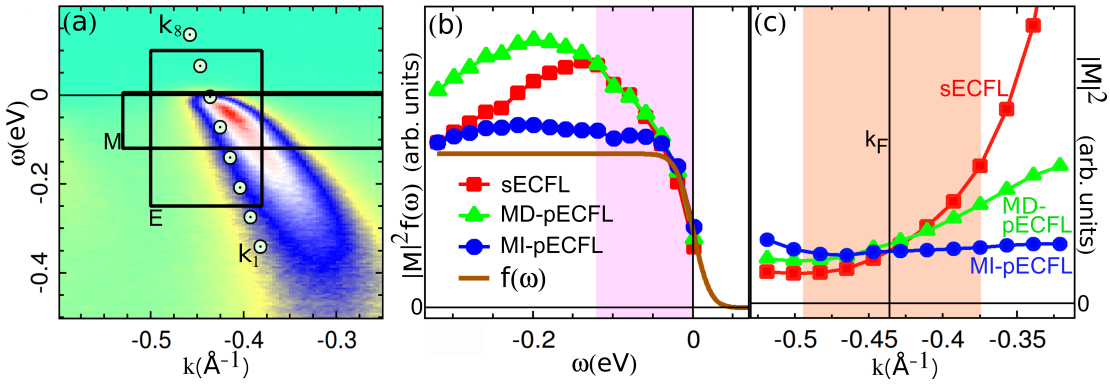

Figure 2.6: The ARPES data for Bi2212 at 91 K, fit in Fig. (2.3) and Fig. (2.4), represented in a false color scale (panel a) and the overall intensity scales used for the MDC fits (panel b) and the EDC fits (panel c). Panels a, b, and c are presented in the same format as panels a, c, and d, respectively, of Fig. 3. As in that figure of the main text, we see that the MI-pECFL model gives the most reasonable values of the overall intensity scales for the MDC fits (panel b) and the EDC fits (panel c), with only a mild dependence of the matrix element on the momentum and the energy, as anticipated.

The success of MI-pECFL model arises crucially from *the separate treatment of the ω dependence and the $\vec{k}$ dependence, or independence, of the caparison factor, important for describing EDCs and MDCs, respectively.*

In contrast to the pECFL models, it is clear that the sECFL model cannot describe MDCs at all. Using identical fit parameters as for EDCs (see the dashed line marked "$\eta = 0.18$ eV" in Fig. 2.2(a)), we get very poor fit quality, which improves, dramatically but insufficiently, by relaxing the η parameter to 0.13 eV (Fig. 2.2(a)). In this new light, the sECFL model, so successful in the previous work [2], must be viewed as getting only one of the two things correct—the ω dependence of the caparison factor, but not its $\vec{k}$ dependence—and its valid regime remains [2] confined to EDCs in the narrow range of $\vec{k}$ around $\vec{k}_F$ (Figs. 2.1(a) and 2.5(a)).

Note that both the MD-pECFL model and the MI-pECFL model agree with the sECFL model, when small energy range and small momentum range are considered, as the EDC fits of Figs. 2.1 and 2.3 show. A more quantitative analysis can be made about this fact, as follows.

As long as the caparison factor defined in Eq. 2.6 is well above zero, the sECFL model remains valid. Using $\gamma_n = 4Q_n\Delta_0/n^2 = 0.38$ eV, determined from our fit parameters, and putting $\omega \approx Z\varepsilon(\vec{k})$, the approximate quasi-particle peak position, we see that Eq. 2.6 requires $(Z-1)\varepsilon(\vec{k}) \lesssim \gamma_n$ in order for $\mathcal{C}_n(\vec{k},\omega) > 0$. Here, we must take Z to be the *total* mass renormalization ratio, which, according to our theory, is equal to $Z = Z_{FL}Q_n = Q_n/3 = 0.19$. Putting these numbers together, we see that the sECFL model is expected to be valid for $\varepsilon(\vec{k}) \gtrsim -0.47$ eV, or $Z\varepsilon(\vec{k}) \gtrsim -0.09$ eV. Noting that $Z\varepsilon(\vec{k})$ corresponds to the approximate peak position in EDC, we therefore learn that the sECFL model would be good for describing EDCs, when their peaks are within about 90 meV from the chemical potential. This explains why sECFL fits are very good in Figs. 2.1 and 2.3, while this is no longer the case in panel (b) in Fig. 2.5. It is for the same reason that MDC fits by the sECFL are very poor.

This consideration explains excellent EDC fits in Ref. ([2]), justifies the simple truncation procedure, $\mathcal{C}_n \to \max(\mathcal{C}_n, 0)$, employed in that work (see panel (e) in Fig. 2.5 also), and, last but not least, correctly puts pECFL models as standing in harmony with the sECFL model, not in contradiction to it.

Now when we come back to the MD-pECFL model, from our discussion up to this point, it does not seem worth much consideration. But, note that neither sECFL

nor MI-pECFL guarantees the fundamental requirement $\mathcal{C}_n(\vec{k},\omega) \geq 0$ (Fig. 2.5(e)). In the MD-pECFL model, we take

$$\gamma_n = \gamma_{n0}\left[1 + \exp\left(\frac{\omega - \varepsilon(\vec{k}) - a_1\gamma_{n0}}{a_2\gamma_{n0}}\right)\right] \tag{2.8}$$

where $\gamma_{n0} \equiv 4Q_n\Delta_0/n^2 = 0.38$ eV is the value of γ_n in the sECFL model. In MD-pECFL, $\mathcal{C}_n(\vec{k},\omega) \geq 0$ *is* guaranteed for any $\vec{k}$ and ω values, if $a_1 \leq 1 + a_2\,(1 - \log a_2)$. Physically, a_1 and a_2 play the role of controlling the MDC asymmetry (Fig. 2.5(f)) and were determined as $a_2 = 2 \pm 1$ and $a_1 = -1 \pm 1$.

The MD-pECFL model is useful to discuss from three points of view. First, its discussion touches upon some basic theoretical issues. Second, it provides an alternative way to define the MI-pECFL model. Third, it provides the best model for the LSCO data as shown in Fig. 2.8.

From Eq. 2.7, the non-negativity of the spectral function requires that $\mathcal{C}_n(\vec{k},\omega) \geq 0$, or equivalently, $\gamma_n \geq \omega - \varepsilon(\vec{k})$. Considering $\varepsilon(\vec{k}) < 0$ and ω near the peak position ($\omega \approx Z\varepsilon(\vec{k})$ where Z is the quasi-particle weight), this leads to the following requirement: $\gamma_n \gtrsim (1 - Z)|\varepsilon(\vec{k})|$. This requirement would clearly be violated for a large value of $|\varepsilon(\vec{k})|$, if γ_n were to be held constant. Going beyond the sECFL approach, where $|\varepsilon(\vec{k})|$ was limited to a small value so that this violation is irrelevant, we can avoid this violation altogether, if we employ a $\vec{k}$ or ω dependent γ_n. In particular, in MD-pECFL,

we take

$$\gamma_n = \gamma_{n0}\left[1 + \exp\left(\frac{\omega - \varepsilon(\vec{k}) - a_1\gamma_{n0}}{a_2\gamma_{n0}}\right)\right]. \tag{2.9}$$

Here, $a_2 > 0$ defines the width ($a_2\gamma_{n0}$) of the sigmoidal drop of $1/\gamma_n$, occurring at a position defined by a_1: $\omega = \varepsilon(\vec{k}) + a_1\gamma_{n0}$. This γ_n function ensures that (1) $\mathcal{C}_n \to Q_n/\omega$ as $\omega \to \infty$, as well as $\omega \to -\infty$, as required by the spectral weight sum rule per $\vec{k}$ within the t-J model, and (2) $A(\vec{k},\omega) \geq 0$ for *any* $\vec{k},\omega$ values, as long as

$$a_1 \leq 1 + a_2\,(1 - \log a_2) \;\equiv\; a_{1,max}(a_2),$$

as can be shown by a bit of algebra, and this way, MD-pECFL ensures the sum rule and the non-negativity of $A(\vec{k},\omega)$.

The new parameters a_1 and a_2 play the role of controlling the MDC asymmetry. Before we discuss this, we must first note that, for a given value of a_2, a_1 has both an upper bound, as just given, and a rough lower bound, $a_1 \gtrsim -a_2$. The lower bound arises due to the empirical fact that the EDC line shape cannot be fit within the AFL theory, which the MD-pECFL theory converges to (up to an overall scale) if $a_1 \to -\infty$. That is, a_1 cannot be too small. These bounds and the line shape fit severely restrict values of a_1 and a_2: a_1 lies at about -1 and a_2 lies at about 2, both with a small wiggle room of about ± 1.

The role of a_1 has been illustrated in panel (f) in Fig. 2.5. As a_1 is tuned from

$-\infty$ to ∞, the MDC goes from completely symmetric, just as in MI-pECFL, to very asymmetric, just as in sECFL.

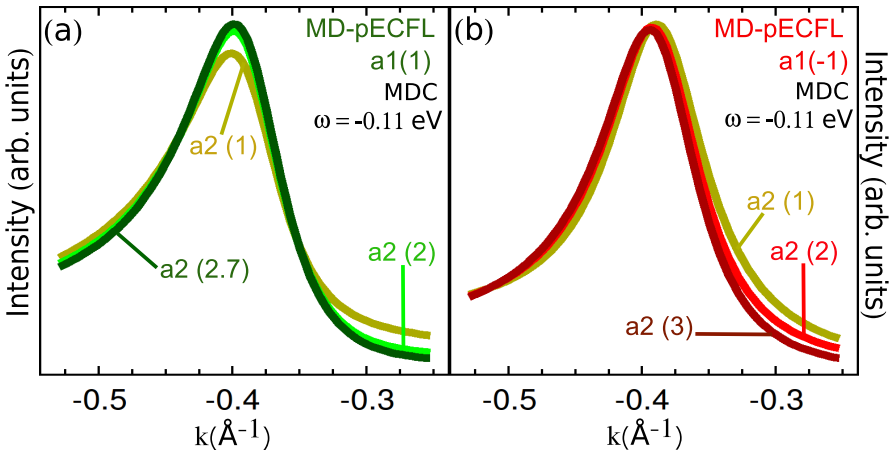

Figure 2.7: The MDC line shape dependence of MD-pECFL on the parameter a_2 at $\omega = -0.11$ eV, (a) $a_1 = 1$, (b) $a_1 = -1$.

In this consideration, the following points are worth noting. First, if $a_1 \to \infty$, then MD-pECFL converges to sECFL. This is because $\gamma_n \to \gamma_{n0}$ in this limit (Eq. 2.8). Second, if $a_1 \to -\infty$, then MD-pECFL does *not* convert to MI-pECFL, but to a "re-weighted" AFL. This is because in this case $\mathcal{C}_n(\vec{k},\omega) \to Q_n$ and $\gamma_n \to \infty$, giving $G(\vec{k},\omega) = Q_n G_{FL}(\vec{k},\omega)$, according to Eqs. 2.5 and 2.6, where G_{FL} is the Green's function for the AFL, as defined right after Eq. 2.7. So, the theory becomes that of the AFL theory, in this limit, except that the total spectral weight is not 1, but the t-J model weight Q_n—so, a "re-weighted" AFL. Now, the MI-pECFL model and the AFL model are quite different, since the caparison factor gives a stronger EDC asymmetry in the former model. However, the two models do have in common that their MDCs are completely symmetric. So, when narrowly focusing on the MDC asymmetry, we

can view the three models—the MI-pECFL model, the AFL model, and the $a_1 = -\infty$ MD-pECFL model—as mutually equivalent.

From this discussion, the following can be noted for the reason why the Bi2212 data are fit poorly by the MD-pECFL model, despite more parameters afforded by it. The combination of the asymmetric EDC behavior and the symmetric MDC behavior displayed by the Bi2212 data pose difficulties to the MD-pECFL model. This is because as the MDC is made more symmetric, the EDC is becoming more symmetric also, contributing the degradation of the fit (panel (b) Fig. 2.1 and Fig. 2.3(b)). Separately, the $a_1 \to -\infty$ MD-pECFL model gives as good an MDC fit as the MI-pECFL model, while the $a_1 = 1$ MD-pECFL model gives as good an EDC fit as the MI-pECFL model. The middle ground is found at $a_1 = -1$, at which value both the EDC fit and the MDC fit suffer a little.

Turning to a_2, Fig. 2.7 shows the dependence of the MDC line shape on a_2. The two constraints—the upper bound and the lower bound of a_1 for a given a_2 value, and vice versa—discussed above mean that the range of a_2 shown here is nearly the full range of a_2 allowed (panel b), or a significant fraction of it (panel a), for each given value of a_1. These line shape changes are of the same kind of line shape change that is controlled by a_1—the change in the MDC asymmetry. Instead of using two parameters to control the same aspect of the data, we found it sufficient to fix the value of a_2 at 2, and use a_1 as a fit parameter to describe the MDC asymmetry. In particular, note that in panel (b), which corresponds to our final a_1 value, the line shape depends little on a_2.

Accordingly, $\mathcal{C}_n$ for MD-pECFL stays clearly above zero and is smooth (Fig. 2.5(e)). $\mathcal{C}_n$ for MI-pECFL is, by definition, that for sECFL at $\varepsilon(\vec{k}) = 0$, as marked by label 1 in Fig. 2.5(e). However, we find that it can also be taken to be that for MD-pECFL at $\varepsilon(\vec{k}) = 0$, as indicated by label 2 in Fig. 2.5(e), since fit results are very comparable between these two choices. Finally, note that, for Bi2212, MD-pECFL is significantly better than sECFL, but significantly worse than MI-pECFL, despite having two more fit parameters.

2.5 ARPES line shape fits of LSCO data

The situation slightly changes when we fit data of $La_{2-x}Sr_xCuO_4$ (LSCO) [19], showing strong MDC asymmetry (panels b–e). Here, identical fit parameter values as those for Bi2212 are used, except for $\eta = 0.12$ eV and v_{F0} (see Sec. 2.3.1). Fig. 2.8(a) shows an EDC fit, good by all models, just as for Bi2212. However, the MDC fit is a different matter. Notably, MDCs show significant asymmetry for $-\omega \gtrsim 0.07$ eV (panel b), and that asymmetry can be described properly only by the MD-pECFL model, as illustrated clearly in fits shown in panels (b) through (e).

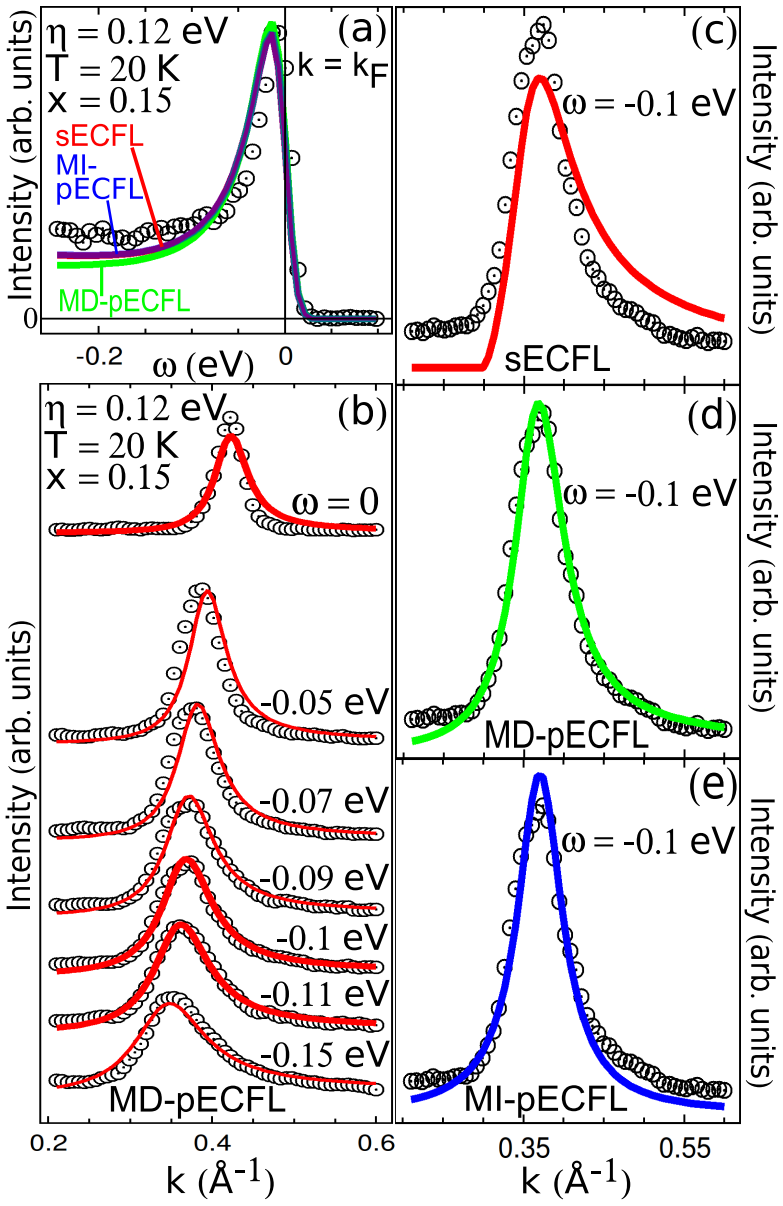

Figure 2.8: Fits to the data of optimally doped ($n = 0.85$; $x = 0.15$) LSCO [19], taken along the nodal direction. (a) EDC fits at $k = k_F$. (b,c,d,e) MDCs for $-\omega \gtrsim 0.07$ eV are significanly asymmetric, described the best by MD-pECFL.

We see that the original sECFL model must be modified greatly (Bi2212) or somewhat (LSCO) to describe MDCs. We argue that these phenomenological modifi-

cations require physics beyond the t-J Hamiltonian, since the sECFL model is derived [1] from the t-J Hamiltonian, and another well-known model [18] based on the t-J Hamiltonian also implies too asymmetric MDCs. More specifically, the physics of the (next nearest neighbor hopping) t' term seems a good candidate: the well-known fact that $|t'/t|$ is significantly smaller for LSCO [20, 21] goes well with our result that the MD-pECFL model is more similar to the sECFL model. The t' term is correlated with the superconducting transition temperature [21], imparting importance to our current proposal. We recently found [22] that an anomalous ARPES feature is explained by pECFL, but not sECFL, and has similarity to a scanning tunneling spectroscopy feature correlated with superconductivity, adding more credence to our argument here. Lastly, the fact that the caparison factor for the infinite-dimensional ECFL becomes $\vec{k}$-independent [23, 24] seems to go along with our result, within the crude analogy between adding a large t' term and increasing channels for t hopping.

2.5.1 Low temperature data

In Fig. 2.9(a), we report the quality of the MDC fits shown in Fig. 2.8, using the standard χ^2 measure of the line shape fit. Perfectly consistent with Figs. 2.8(c–e), we see that the χ^2 values for the sECFL model is much too high compared to the χ^2 values for the two pECFL models. This lends a definite support to the pECFL model. However, which pECFL model is better?

As Fig. 2.9(a) shows, the χ^2 value is smaller for the MI-pECFL model at low energy ($-\omega \lesssim 0.05$ eV), while it is smaller for the MD-pECFL model for ($-\omega \gtrsim 0.05$

eV). So, our question above can be rephrased as "which of these two facts is more significant?" The answer is the latter, since the theory that we are applying here is applicable only to physics in the high temperature scale or the high energy ($-\omega$) scale. When we examine the low temperature data, and compare the data with the theory for the normal state at high temperature, our primary concern must be focused on the high energy ($-\omega$) behavior.

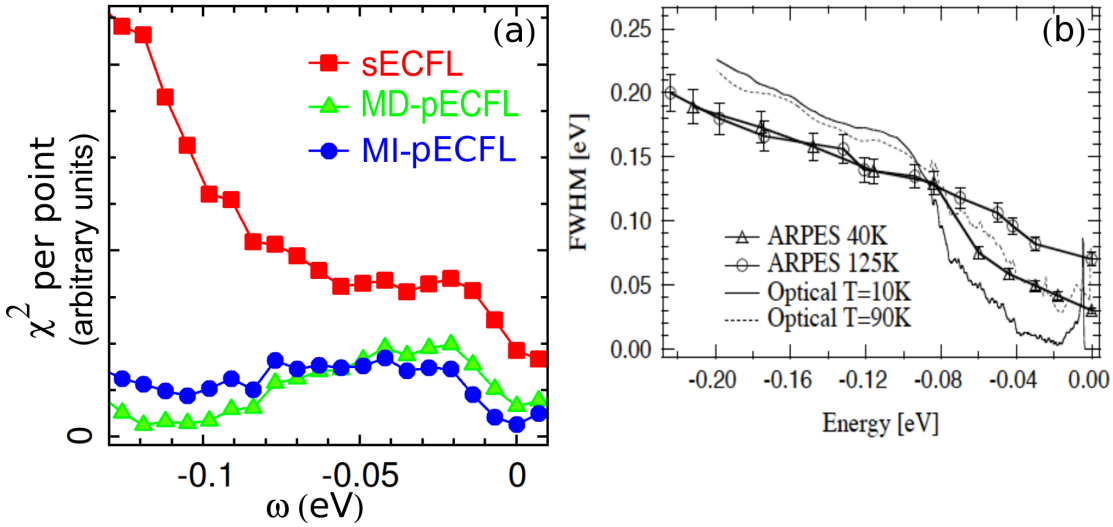

Figure 2.9: (a) χ^2 per point for the three models used for the line shape analysis of LSCO (20K) in Fig. 2.8. (b) The FWHM values of MDCs for an optimally doped Bi2212 ($T_c = 90$ K), as reported by Kaminski et al., in Fig. 4 of their paper, Phys. Rev. Lett. **84**, 1788 (2000). Also included are the carrier scattering rate from infrared reflectivity measurements (A. V. Puchkov, et al., J. Phys. Cond. Matt. **8**, 10049 (1996)).

This view point is also supported well empirically by the known results of the literature. For instance, in Fig. 2.9(b), we show a plot taken from a reference, given in the caption. This plot shows that the FWHM values of the ARPES data are nearly temperature independent at high energy, $-\omega \gtrsim 0.08$ eV. This is due to the fact that the high energy data taken at low temperatures are essentially identical with the high

energy data taken at high temperatures.

This fact justifies our use of the low temperature data in Fig. 2.8. It also guides us importantly to assess the relative merits of the two models, MD-pECFL and MI-pECFL, for the LSCO data. Focusing on high energy, we conclude that the MD-pECFL model is much better, as its χ^2 value is several times smaller than that for MI-pECFL at high energy $-\omega \gtrsim 0.05$ eV (Fig. 2.9(a)).

This does not mean that we do not need to study the high temperature data for LSCO. On the contrary, the current lack of the high temperature data for LSCO in view of our current result makes the study of high temperature ARPES data for LSCO a very attractive topic. In view of the success of the ECFL model, the strong temperature dependence predicted at high temperatures (Fig. 5(f) of Ref. ([2])), and the apparent difference between the LSCO data and the Bi2212 data, the investigation of the high temperature ARPES line shapes for LSCO may be an excellent topic of research in the near future.

Lastly, note that at low temperatures, the low energy ARPES peak is significantly sharper than our theoretical model predicts, as the MDC comparison at $\omega = 0$ in Fig. 2.8(b) or Fig. 2.4(c) shows. This seems consistent with the general notion that the onset of the superconducting gap (or pseudo-gap) reduces the decay channels for quasi-particles.

2.6 Conclusion

In conclusion, we proposed a phenomenological ARPES line shape model, based on the ECFL theory [1, 15]. The essential feature of our model remains the caparison factor [1, 2, 16], which is capable of describing both anomalous EDC line shapes [18, 2], universal for high T_c cuprates, and apparently more conventional MDC line shapes [12, 13]. While our model is not the first to fit both EDCs and MDCs [12] of high T_c cuprates, its demonstrated fidelity (including a qualitative description of $|M_{if}|^2$) and range of applicability is now unprecedented. Also unprecedented is the notable fact that our model requires a Dyson self energy [25], whose form is *drastically different from that assumed by the prevalent, but incomplete, MDC-only analysis* [26, 27]: to our knowledge, ours is the only $\vec{k}$-dependent [25] Dyson self energy that has fit cuprate MDCs. Thus, extending the current analysis to wider ranges of momentum, doping, and temperature and studying its implication on other properties such as the resistivity [16] seems to make a great research topic for the immediate future.

Chapter 3

Origin of Kinks in Energy Dispersion of Strongly Correlated Matter

This chapter reproduces, Kazue Matsuyama, Edward Perepelisky, and B. Sriram Shastry, "Origin of Kinks in Energy Dispersion of Strongly Correlated Matter." arXiv preprint arXiv:1610.08079 (2016). The manuscript is currently under consideration for publication.

3.1 Abstract

We investigate the origin of ubiquitous low energy kinks found in Angle Resolved Photoemission (ARPES) experiments in a variety of correlated matter. Such kinks are unexpected from weakly interacting electrons and hence identifying their origin should lead to fundamental insights in strongly correlated matter. We devise a protocol for extracting the kink momentum and energy from the experimental data which relies solely on the two asymptotic tangents of each dispersion curve, away from

the feature itself. It is thereby insensitive to the different shapes of the kinks as seen in experiments. The body of available data is then analyzed using this method. We proceed to discuss two alternate theoretical explanations of the origin of the kinks. Some theoretical proposals invoke local Bosonic excitations (Einstein phonons or other modes with spin or charge character), located exactly at the energy of observed kinks, leading to a *momentum independent* self energy of the electrons. A recent alternate is the theory of extremely correlated Fermi liquids (ECFL). This theory predicts kinks in the dispersion arising from a *momentum dependent* self energy of correlated electrons. We present the essential results from both classes of theories, and identify experimental features that can help distinguish between the two mechanisms. The ECFL theory is found to be consistent with currently available data on kinks in the nodal direction of cuprate superconductors, but conclusive tests require higher resolution energy distribution curve data.

3.2 Introduction

High precision measurements of electronic spectral dispersions has been possible in recent years, thanks to the impressive enhancement of the experimental resolution in the angle resolved photoemission spectroscopy (ARPES). This technique measures the single electron spectral function $A(\vec{k}, \omega)$ multiplied by the Fermi occupation function; it can be scanned at either fixed $\vec{k}$ as a function of ω or at fixed ω as a function of $\vec{k}$. These scans produce respectively the energy distribution curves (EDCs) and momentum

distribution curves (MDCs). The line shapes in both these scans are of fundamental interest, since they provide a direct picture of the quasiparticle and background components of interacting Fermi systems, and thus unravel the roles of various interactions that are at play in strongly correlated Fermi systems. The dispersion relation of the electrons can be studied through the location of the peaks of $A(\vec{k},\omega)$ in constant ω or constant $\vec{k}$ scans, and recent experimental studies have displayed a surprising ubiquity of "kinks" in strongly correlated matter at low energies $\sim 50-100$ meV. The kinks are bending type anomalies (see Fig. (3.1)) of the simple linear energy versus momentum dispersion, expected near $\vec{k}_F$ from band theory. It is evident that the kinks arise from some departure from band theory- through mutual interactions or with other degrees of freedom. Elucidating their origin is of basic importance, and is the main goal of this work.

The purpose of this paper is multifold, we (i) survey the occurrence of the kinks in a variety of correlated systems of current interest, (ii) provide a robust protocol for characterizing the kinks which is insensitive to the detailed shape of the kink, (iii) discuss how these kinks arise in two classes of theories, one based on coupling to a Bosonic mode and the other to strong correlations, and (iv) identify testable predictions that ARPES experiments can use to distinguish between these.

The fifteen systems reporting kinks are listed in Table (3.1); these include (1) most high T_c cuprates in the (nodal) direction $\langle 11\rangle$ at various levels of doping from insulating to normal metallic states in the phase diagram [28, 29] (2) charge density wave systems, (3) cobaltates and (4) ferromagnetic iron surfaces. The kinks lose their

sharpness as temperature is raised [30, 29, 31], and appear to evolve smoothly between the d-wave superconducting state and the normal state.

Name of the compounds					Local Bosonic Mode		
	Above Tc		Below Tc				
	MDC	EDC	MDC	EDC	Charge	Spin	Not reported
LSCO	✓[30, 36]		✓[30, 28, 19, 36]	✓[37]	✓[38, 39, 40]	✓[41]	
Bi2201	✓[30, 36, 32, 42]	✓[43]	✓[32]		✓[44]		
Bi2212	✓[45, 29, 30, 31, 32, 36]	✓[31]	✓[29, 30, 31, 32, 36]		✓[46]	✓[47, 48]	
Bi2223	✓[32, 49]		✓[32, 49, 50]				✓
YBCO			✓[51]		✓[52, 53]	✓[54, 55, 56, 57]	
Hg1201			✓[58]		✓[59]	✓[60, 61, 62]	
F0234			✓[63]				✓
CCOC			✓[64]				✓
LSMO			✓[65]	✓[65]			✓
2H-TaSe2 (CDW)			✓[66]		✓[67]		
Iron (110) surface			✓[68] 85 K				✓
BiBaCo1			✓[69] 5K	✓[69] 5K			✓
BiBaCo2			✓[69] 5K	✓[69] 5K			✓
BiBaCo	✓[69] 200K	✓[69] 200K					✓
NaCoO			✓[69] 5K	✓[69] 5K			✓

Table 3.1: Comprehensive survey for ARPES kinks

The kinks above T_c are smoothed out as one moves away from nodal direction [32]. Recent experiments [33] resolve this movement of the kinks more finely into two sub features. Most of the studies in Table (3.1) focus on MDC's, the EDC data is available for only eight systems so far. Bosonic modes have been reported in six systems using different probes such as inelastic x-rays or magnetic scattering, with either charge (phonons, plasmons) or spin (magnetic) character, while the remaining nine systems do not report such modes. A few theoretical studies of the kinks have implicated the observed low energy modes via electron-Boson type calculations; we summarize this calculation in Sec. 3.7. We find, in agreement with earlier studies, that the Boson coupling mechanism yields kinks in the MDC dispersion, provided the electron-Boson coupling is taken to be sufficiently large. In addition, we find in all cases studied, this mechanism also predicts a jump in the EDC dispersion. It also predicts an extra peak in the spectral function pinned to the kink energy after the wave vector crosses the kink. These two features are experimentally testable and differ from the predictions of the correlations mechanism discussed next.

Since kinks are also observed in cases where no obvious Bosonic mode is visible, it is important to explore alternate mechanisms that give rise to such features. In this context we note that a recent theoretical work using the extremely strongly correlated Fermi liquid (ECFL) theory [1, 34] calculates the dispersion using a low momentum and frequency expansions of the constituent self energies. This calculation [34] shows that both EDC and MDC energy dispersions display qualitatively similar kinks, in particular there is no jump in either dispersion. In essence this work implies that a purely electronic

mechanism with a strong momentum dependence of the Dyson self energy results in kink type anomalies. We provide some details of this theoretical calculation, and identify features that can be tested against the experiments. In terms of parameter counting, the calculation is *overdetermined*, it can be represented in terms of four parameters which can be fixed from a subset of measurements. With this determination one can then predict many other measurables and testable relations between these- as we show below. We show below that the various predictions are reasonably satisfied in one case (of OPT Bi2212 below), while in other cases, there is insufficient experimental data to test the theories.

Some details of the current status of the ECFL theory can be found in Sec. 3.8. The ECFL theory incorporates strong Gutzwiller type correlation effects into the electron dynamics. It produces line shapes that are in close correspondence to experimental results for the high T_c systems [2, 3]. The presence of a low energy kink in the theoretical dispersion was already noted in Ref. ([2]), the present work substantially elaborates this observation. In order to understand the origin of a low energy scale in the ECFL theory, it is useful to recall the predicted cubic correction to Fermi liquid self energy $\mathrm{Im}\, m\, \Sigma(\vec{k}_F, \omega) \sim \omega^2(1 - \frac{\omega}{\Delta_0})$ from equations (3.45, 3.7, 3.8). Here Δ_0 is an emergent low energy scale, it is related to the correlation induced reduction of the quasiparticle weight Z. It reveals itself most clearly in the observed particle hole asymmetry of the spectral functions, and therefore can be estimated independently from spectral *lineshape* analysis. A related and similar low value of the effective Fermi temperature is found in recent studies of the resistivity [35]. Here and in our earlier studies it is coincidentally

found that $\Delta_0 \sim 20 - 50$ meV, i.e. it is also roughly the energy scale of the kinks when the bandwidth is a few eV.

3.3 ARPES spectral dispersions, kinks and a protocol for data analysis

3.3.1 Summary of variables in the theory

A few common features of spectral dispersions found in experiments are summarized in Fig. (3.1). The schematic figure shows a region of low spectral velocity near the Fermi momentum followed by a region of steeper velocity, these are separated by a bend in the dispersion- namely the kink. While the kink itself has a somewhat variable shape in different experiments, the "far zone" is much better defined and is usually independent of the temperature, we denote the velocities in the far zones V_L, V_H for MDC and their EDC counterparts by V_L^*, V_H^*. In terms of the normal component of the momentum measured from the Fermi surface $\hat{k} = (\vec{k} - \vec{k}_F).\vec{\nabla}\varepsilon_{k_F}/|\vec{\nabla}\varepsilon_{k_F}|$, the kink momentum $\hat{k}_{kink}$ is uniquely defined by extrapolating the two asymptotic tangents, and the binding energy at this momentum defines the ideal kink energy E_{kink}^{ideal} (see Eq. (3.6)), which serves as a useful reference energy.

We first define the important ratio parameter r $(0 \leq r \leq 2)$ from the MDC dispersion velocities as

$$r = \frac{2V_H}{V_H + V_L}. \tag{3.1}$$

The EDC and MDC dispersion relation $E^*(k)$ and $E(k)$ are found from theory (see Sec. 3.8 and Ref. ([34])) as:

$$E^*(k) = \left(r\, V_L \hat{k} + \Delta_0 - \sqrt{\Gamma_0^2 + Q^2} \right), \tag{3.2}$$

$$E(k) = \frac{1}{2-r} \left(V_L \hat{k} + \Delta_0 - \sqrt{r(2-r)\,\Gamma_0^2 + Q^2} \right), \tag{3.3}$$

where we introduced an energy parameter related to r, V_L and $\hat{k}_{kink}$

$$\Delta_0 = \hat{k}_{kink} V_L (1-r), \tag{3.4}$$

and a momentum type variable $Q = (r-1)\, V_L\, (\hat{k} - \hat{k}_{kink})$. The variable Γ_0 is temperature like,

$$\Gamma_0 = \eta + \pi \{\pi k_B T\}^2 / \Omega_\Phi; \tag{3.5}$$

here η is an elastic scattering parameter dependent upon the incident photon energy, it is very small for laser ARPES experiments and can be neglected to a first approximation. Further, Ω_Φ a self energy decay constant, is explained further in Sec. 3.8. The ideal kink energy $V_L \hat{k}_{kink}$ can be expressed in terms of Δ_0 scale as:

$$E_{kink}^{ideal} = -\frac{1}{r-1} \Delta_0. \tag{3.6}$$

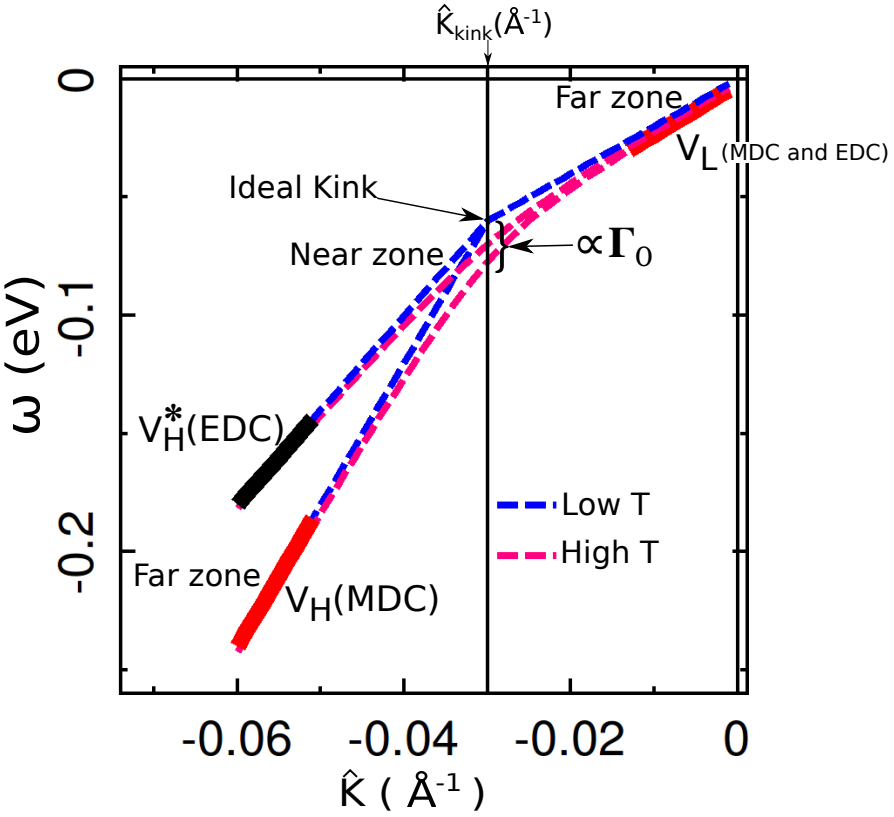

Figure 3.1: A schematic MDC and EDC spectrum displaying typical features of experiments discussed below. Here $\hat{k} = (\vec{k} - \vec{k}_F).\vec{\nabla}\varepsilon_{k_F}/|\vec{\nabla}\varepsilon_{k_F}|$, is the momentum component normal to the Fermi surface, and we label EDC variables with a star. (The sketch uses parameters $\mathrm{V_L} = 2\,\mathrm{eV}\,\mathring{A}$, $\mathrm{V_H} = 6\,\mathrm{eV}\,\mathring{A}$, $r = 1.5, \hat{k}_{kink} = -0.03\,\mathring{A}^{-1}$, $\Delta_0 = 0.03\,\mathrm{eV}$, and $\Gamma_0 = 0.01\,\mathrm{eV}$ in equation (3.2,3.3)). The tangents in the *far zones* identify the asymptotic velocities $V_L < V_H$ and $V_L^* < V_H^*$ that characterize the MDC and EDC spectra. The intersection of the extrapolated MDC tangents fixes the kink momentum $\hat{k}_{kink}$ and the ideal energy E_{kink}^{ideal}. The dispersion is rounded with raising T, as in the lower (red) curve. We *define* the MDC kink energy E_{kink}^{MDC} as $E(\hat{k}_{kink})$, i.e. the binding energy measured *at* the kink momentum, and similarly the EDC kink energy. In all cases $V_L = V_L^*$. A testable consequence of the ECFL theory is that V_H^* is fixed in terms of the two MDC velocities by a strikingly simple relation: $V_H^* = \frac{3V_H - V_L}{V_H + V_L} \times V_L$. This prediction is tested against experimental data in Fig. (3.2) where both EDC and MDC data is available. In contrast the electron-Boson theory predicts a jump in the EDC dispersion at the kink energy, followed by $V_H^* = V_H$. Note that the difference between the EDC (MDC) kink energy and the ideal kink energy is equal (proportional) to Γ_0 (see Eqs. (3.9) and (3.10)).

The spectral function at low frequencies close to $\vec{k}_F$ is also obtainable from these parameters, the relevant formula is noted below. In terms of ξ

$$\xi = \frac{1}{\Delta_0}(\omega - r\, V_L \hat{k}) \tag{3.7}$$

the spectral function is:

$$A(\vec{k},\omega) = \frac{z_0}{\pi}\frac{\Gamma_0}{(\omega - V_L\hat{k})^2 + \Gamma_0^2} \times \{1 - \frac{\xi}{\sqrt{1 + c_a\xi^2}}\}, \tag{3.8}$$

Here z_0 is the quasiparticle weight and $c_a \sim 5.4$ (see Sec. 3.8). We should keep in mind that these expressions follow from a low energy expansion, and is limited to small $\hat{k}$ and ω; in practical terms the dimensionless variable $|\xi| \lesssim 4$, so that ω (or $\hat{k}$) is bounded by the kink energy (or momentum), as defined below.

3.3.2 Fixing the parameters

The independent parameters in the ECFL expressions for the kink can be taken as $V_H, V_L, \hat{k}_{kink}$ and Γ_0. These can be fixed with four measurements as we indicate below. While the first three can be measured with precision, the variable Γ_0 depends on the temperature and is also quite sensitive to the various experimental conditions including the incident photon energy, thus making it less precisely known than the others; we will perforce be content with rough estimates of this variable. The remaining parameters can be calculated using Eq. (3.1) and Eq. (3.4) etc. As mentioned above, the theory

is overdetermined, in terms of these four parameters, the theory predicts a number of other quantities: a) the dispersion curves for both EDCs and MDCs, b) the location of both EDC and MDC kinks at finite temperature, and c) the spectral functions near the Fermi level (up to roughly the kink energy). Below we present an analysis of the ARPES data of Bi2212, LSCO and Bi2201 taken from literature, where we give the details of the fits and the predicted EDC velocities for future experiments.

The asymptotic velocities V_H, V_L determine the ratio r from Eq. (3.1). The energy Δ_0 and the ideal kink energy are determined from equations (3.4, 3.6). As discussed in Fig. (3.1) E_{kink}^{MDC} is found by measuring the dispersion at the kink wave vector $E(\hat{k}_{kink})$, and similarly the EDC kink energy E_{kink}^{EDC} is found from $E^*(\hat{k}_{kink})$. For understanding the finite temperature data, the theory provides temperature dependent correction terms for the two spectra, determined by the parameter Γ_0 (see Sec. 3.8),

$$E_{kink}^{EDC} = E_{kink}^{ideal} - \Gamma_0, \tag{3.9}$$

$$E_{kink}^{MDC} = E_{kink}^{ideal} - \Gamma_0 \sqrt{\frac{r}{2-r}}. \tag{3.10}$$

Since Γ_0 determines the non-zero T (or η) correction, we estimate from the difference between low and high temperature MDC dispersion curves

$$\Gamma_0 = \Delta E_{kink} = \sqrt{\frac{2-r}{r}} \left(E_{kink}^{ideal} - E_{kink}^{MDC} \right). \tag{3.11}$$

Clearly uncertainties in Γ_0 are governed by those in the MDC dispersion at the kink

momentum.

As noted in Fig. (3.1), the ECFL theory predicts a kink, rather than a jump in the EDC spectrum, quite analogous to that in the MDC dispersion, but with a different velocity on the steeper side, i.e. $V_H^* \neq V_H$. In fact the theory provides an experimentally testable expression relating the two, V_H^* is expressed quite simply in terms of measurable experimental variables,

$$V_H^* = \frac{3V_H - V_L}{V_H + V_L} \times V_L. \tag{3.12}$$

As mentioned in the introduction the Boson-mode coupled theories predict a jump in the EDC spectrum at the kink energy. The velocity beyond the jump is the same in EDC and MDC, i.e. $V_H^* = V_H$, in contrast to Eq. (3.12). This velocity is reported in only a few cases, and provides a ready test of the ECFL theory.

The theory also predicts $V_L = V_L^*$, which is satisfied by inspection in all reported cases and is common to the Boson-mode theory. We use this protocol to analyze the experiments on three well studied families of high T_c materials next.

3.4 OPT Bi2212 ARPES dispersion data

In the well studied case of optimally doped Bi2212 (BSCCO) superconductors, the kink has been observed in both EDC and MDC. We summarize the ECFL fit parameters in Table (3.2) obtained from literature [31]. We also display the predicted energy and velocity of the EDC spectral kink. The velocity ratio $V_H/V_H^* \sim 1.3$ in this

case, is quite large and measurable. In this case the EDC dispersion has fortunately already been measured, allowing us to test the prediction. From Table (3.2) we see that the energy of the EDC kink and its velocity are close to the predictions.

MDCs					EDCs			
OPT Bi2212 ARPES data			E_{kink}^{MDC}(meV)		E_{kink}^{EDC}(meV)		V_H^* (eV $\mathring{A}$)	
V_L (eV $\mathring{A}$)	V_H (eV $\mathring{A}$)	$\hat{k}_{kink}$ ($\mathring{A}^{-1}$)	Calculated	Measured	Calculated	Measured	Predicted	Measured
1.47 $\pm$0.07	3.3 $\pm$ 0.3	- 0.037 $\pm$ 0.005	67 $\pm$ 21	67 $\pm$ 8	63 $\pm$ 21	65 $\pm$ 8	2.60 $\pm$ 0.56	2.1 $\pm$ 1.1

Table 3.2: Parameter table for ARPES kink analysis for OPT Bi2212 [31] in Fig. 3.2 presents three essential parameters, V_L, V_H, and $\hat{k}_{kink}$. From the high and low temperature MDC dispersions, we measured $\Gamma_0 \lesssim 10$ meV in Panel (b) of Fig. 3.2. With the measured experimental parameters and determining the velocity ratio r in Eq. (3.1), we are able to estimate the finite temperature kink energy for EDC and MDC dispersions by Eq. (3.9) and Eq. (3.10) and predict V_H^* by Eq. (3.12). The uncertainties for calculated variables were determined by error propagation, and the uncertainties for experimental variables were given by the half of the instrumental resolution.

In Panel (a) in Fig. 3.2, we plot the predicted EDC dispersion using the parameters extracted from the MDC dispersion in Panel (b), and compare with the ARPES data measured[31]. It is interesting that the predicted slope of the EDC dispersion from Eq. (3.12) is close to the measured one. Indeed the measured EDC dispersion is close to that expected from the ECFL theory. To probe further, in Panel (c) in Fig. (3.2) we compare the theoretical EDC line shape (solid blue line) given by the same parameters through Eq. (3.8), with the ARPES line shape measured at high temperature [31].

Panel (d) compares the theoretical MDC curve with the data. The theoretical curves are from the low energy expansion and hence are chopped at the high end, corresponding to roughly $|\xi|_{max} \sim \frac{r\,\mathrm{V_L}\,\hat{k}_{kink}}{\Delta_0}$ for MDC and $|\xi|_{max} \sim \frac{E^{ideal}_{kink}}{\Delta_0}$ for the EDC. With this cutoff, the momentum is less than the kink momentum and the energy is less than the kink energy. We used $\Gamma_0 = 40$ meV since it provides a rough fit for both EDC and MDC spectral functions.

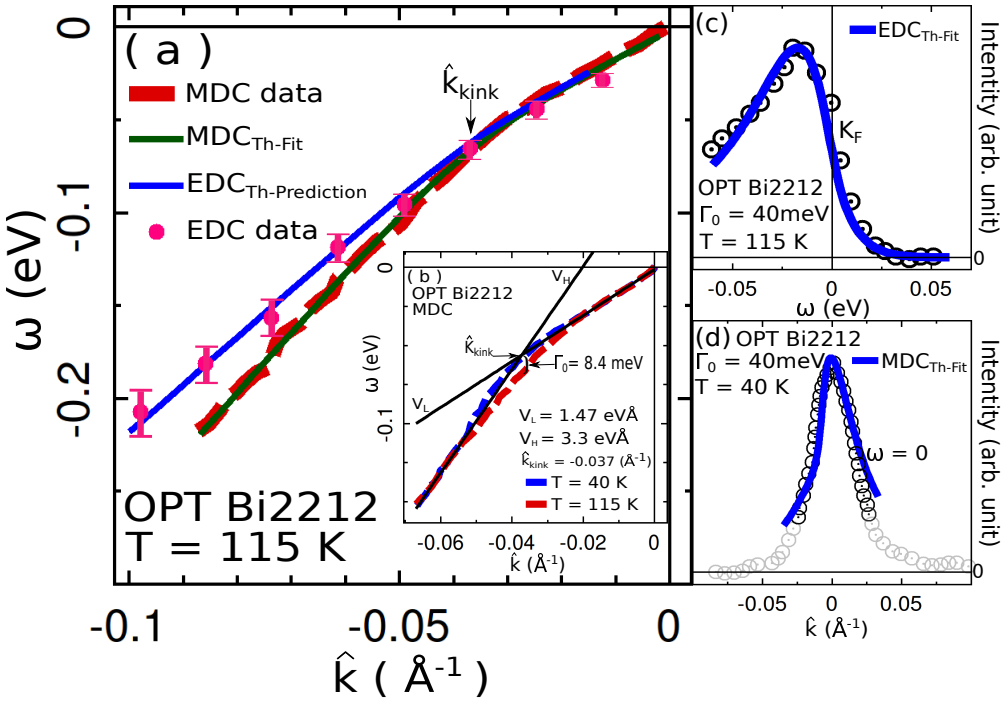

Figure 3.2: ARPES kinks data for OPT Bi2212 from Ref. ([31]) compared to theoretical ECFL curves (solid lines) using parameters listed in Table. 3.2. **Panel:(a)** The predicted EDC spectrum (blue) from Eq. (3.2), versus the experimental EDC data (magenta symbols) at T=115K. For reference we also show the MDC data (red dashed curve) and the corresponding ECFL fit (green solid curve). **Panel:(b)** Experimental MDC spectra at 40K (below T_c in blue dashed line) and 115K (above T_c in red dashed line) yield common asymptotes shown in black lines from the far zone. These determine the parameters displayed in Table (3.2). **Panel:(c)** At low energy ± 60 meV, the EDCs spectral function (blue solid line) from Eq. (3.8) is contrasted with the corresponding ARPES data from [31]. **Panel:(d)** At $\omega = 0$ we compare the MDCs spectral function (blue solid line) from Eq. (3.8) with the corresponding ARPES data from Ref. ([31]). The range of validity for the theoretical expansion is $\pm\, \hat{k}_{kink}$ ($0.037 \mathring{A}^{-1}$), the data points in the range are shown in black circle symbols, while the light gray circle symbols are outside this range. The peak position of the theoretical curve has been shifted to left by $0.007\, \mathring{A}^{-1}$ which is within the instrumental resolution of $0.01\, \mathring{A}^{-1}$.

This value is somewhat larger than the bound ~ 10 meV given in Table (3.2), a smaller value leads to narrower lines but with the same shape. In rigorous terms the same Γ_0 must fit the dispersion and also the spectral functions. Our fit, requiring a different Γ_0, is not ideal in that sense. However the resolution of the available data is somewhat rough, and should improve with the newer experimental setups that have become available. We thus expect that higher resolution data with laser ARPES should provide an interesting challenge to this theory. We also stress that from Eq. (3.8), the MDC curves look more symmetric than the EDC curves at low energies. While many experimental results do show rather symmetric MDC's, there are well known exceptions. For instance MDCs asymmetry has indeed been reported for nearly optimally doped Hg1201 (Tc = 95 K) at binding energy very close to the Fermi level, $\omega \sim$- 5 meV and $\omega \sim$-18 meV in Fig. 5 in Ref. ([58]).

Note that the $\omega = 0$ MDC plot of the spectral function $A(k, \omega)$ from Eq. (3.8), locates the peak momentum $\hat{k}_{peak} > 0$, i.e. slightly to the right of the physical Fermi momentum $\vec{k}_F$. This implies that the *experimental* Fermi momentum determination is subject to such a correction, whenever the spectral function Eq. (3.8) has a momentum dependent caparison factor. In the case displayed in Panel (d), the shift is $0.007\,\mathring{A}^{-1}$, a bit less than the instrumental resolution, and we have shifted the curve to the *left* for comparing with the data. A similar shift is made in Panel (l) Fig. 3.3. For analogous reasons the EDC peak in $A(k, \omega)$ at $\vec{k}_F$ is shifted to the left i.e. $\omega_{peak} < 0$. A small shift to the *right* is made in Panel (k) of Fig. (3.3), in order to compensate for this effect. These shift effects are within the resolution with present setups, but should be

interesting to look for in future generation experiments, since they give useful insights into the energy momentum dependence of the spectral function.

3.5 LSCO low temperature data

Here we analyze the LSCO data at low temperature (20 K) and at various doping levels raging from the insulator (x = 0.03) to normal metal (x = 0.3) from Ref. ([28]). The parameters are listed in Table (3.3), where we observe that the velocity V_L is roughly independent of x, and has a somewhat larger magnitude to that in OPT Bi2212 in Table (3.2). The kink momentum decreases with decreasing x, roughly as $\hat{k}_{kink} = -(0.37x - 0.77x^2)\mathring{A}^{-1}$, and the kink energies of EDC and MDC dispersions are essentially identical. In the region beyond the kink, the prediction for V_H^* is interesting since it differs measurably from the MDC velocity V_H. We find the ratio $V_H/V_H^* \sim 1.02 - 1.5$ is quite spread out at different doping.

MDCs						EDCs			
LSCO low temperature ARPES data				E_{kink}^{MDC}(meV)		E_{kink}^{EDC}(meV)		V_H^* (eV Å)	
x (doping level)	V_L (eV Å)	V_H (eV Å)	$\hat{k}_{kink}$ ($Å^{-1}$)	Calculated	Measured	Calculated	Measured	Calculated	Measured
0.3	2.4 ± 0.2	3.0 ± 0.3	-0.047 ± 0.005	113 ± 29	110 ± 10	113 ± 29		2.93 ± 0.45	
0.22	2.0 ± 0.1	3.6 ± 0.2	-0.042 ± 0.005	84 ± 18	85 ± 10	84 ± 18		3.14 ± 0.35	
0.18	1.7 ± 0.3	4.5 ± 0.6	-0.040 ± 0.005	68 ± 43	72 ± 10	68 ± 43		3.2 ± 1.2	
0.15	1.75 ± 0.07	4.3 ± 0.1	-0.037 ± 0.005	65 ± 11	64 ± 10	65 ± 11		3.23 ± 0.20	
0.12	2.0 ± 0.3	3.7 ± 0.5	-0.029 ± 0.005	58 ± 28	55 ± 10	58 ± 28		3.19 ± 0.89	
0.1	1.8 ± 0.2	5.0 ± 0.7	-0.035 ± 0.005	63 ± 44	64 ± 10	63 ± 44		3.5 ± 1.4	
0.075	1.9 ± 0.2	5.6 ± 0.8	-0.026 ± 0.005	49 ± 37	51 ± 10	49 ± 37		3.8 ± 1.7	
0.063	1.8 ± 0.3	6.0 ± 0.5	-0.022 ± 0.005	40 ± 21	43 ± 10	40 ± 21		3.7 ± 1.1	
0.05	1.7 ± 0.2	5.7 ± 0.6	-0.023 ± 0.005	39 ± 25	41 ± 10	39 ± 25		3.5 ± 1.3	
0.03	2.0 ± 0.3	6.1 ± 0.4	-0.016 ± 0.005	32 ± 15	32 ± 10	32 ± 15		4.02 ± 0.85	

Table 3.3: Data table for ARPES kink analysis for OPT LSCO (T = 20 K) [28] in Fig. 3.3. We were unable to reliably estimate Γ_0 here due to the lack of data at high temperature, and hence set it at zero. The uncertainties for measured values were given by half of the instrumental resolution (10 meV, $\sim 0.005\, Å^{-1}$). The uncertainties for the calculated values were determined by error propagation.

Our analysis becomes unreliable as lower doping level x < 0.075 in Panels (h) to (j) in Fig. 3.3, where the dispersion kink is no longer a simple bending kink, an extra curving tendency begins to appear. To put this in context, recall that the line shape of LSCO becomes extremely broad at small x [19], and so the peak position of the spectral function becomes more uncertain than at higher energy. We should

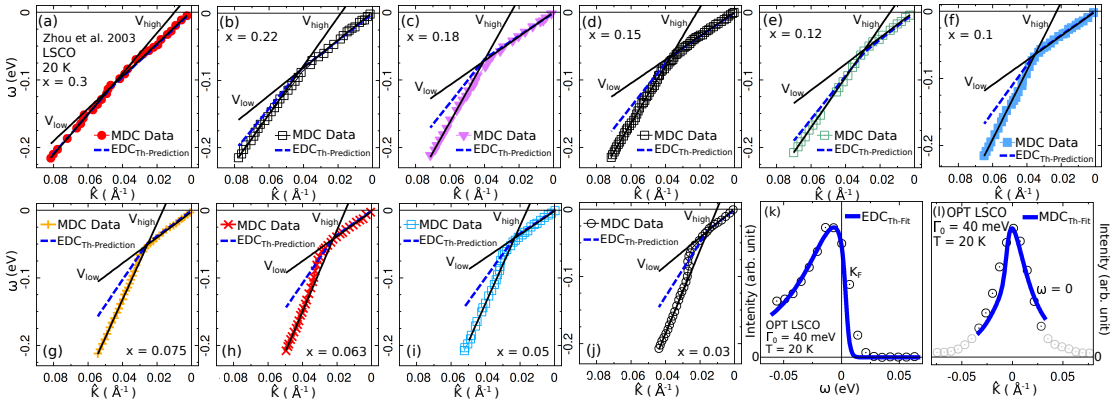

Figure 3.3: ARPES kinks data for LSCO data [28] compared to theoretical ECFL curves (solid lines) using parameters listed in Table. 3.3. The doping level x varies between (normal metal) $0.3 \leq$ x ≤ 0.03 (insulator) in Panels (a) to (j). Each panel shows MDC nodal dispersion data (symbols), whose uncertainties are $\pm$ 10 meV. Two black solid straight lines represent V_L and V_H, and the blue dashed line is the theoretical prediction for EDC dispersion by Eq. (3.2). **Panel:(k)** We compare the spectral line shape for EDCs at k_F from Eq. (3.8) (blue solid line) in the range $\pm E^{ideal}_{kink} \sim$ 65 meV with the corresponding ARPES data (black circles) [3]. **Panel:(l)** At $\omega = 0$ we compare the MDCs spectral function (blue solid line) from Eq. (3.8) with the corresponding ARPES data from Ref. ([3]). The range of validity for the theoretical expansion is $\pm \hat{k}_{kink}$ ($0.037 \mathring{A}^{-1}$), the data points in the range are shown in black circle symbols, while the light gray circle symbols are outside this range. The peak position of the theoretical curve MDC has been shifted to left by $0.006\, \mathring{A}^{-1}$.

point out that in Fig. (3.3) Panel (k) the spectral function has been shifted to right by 4 meV for a better fit. This shifting is consistent with our argument that the Fermi momentum determination has a possible small error of in order $0.006\, \mathring{A}^{-1}$, arising

from the $\hat{k}$ dependent caparison factor, and hence the peak position has an uncertainty $V_L \times .006 \sim 10$ meV.

3.5.1 Fit parameters

For the LSCO data, we quoted the ECFL theory parameters, velocity ratio r, the ideal kink energy E_{kink}^{ideal} and the small energy parameter Δ_0, in Eqs (1,6,4) (see also Eq. (3.36)). In Fig. 3.4, we display the doping dependence of these parameter $x = 1-n$. The size of the data point represent the uncertainty for each data points. While r and Δ_0 stay almost constant, the ideal kink energy decreases linearly with increasing x.

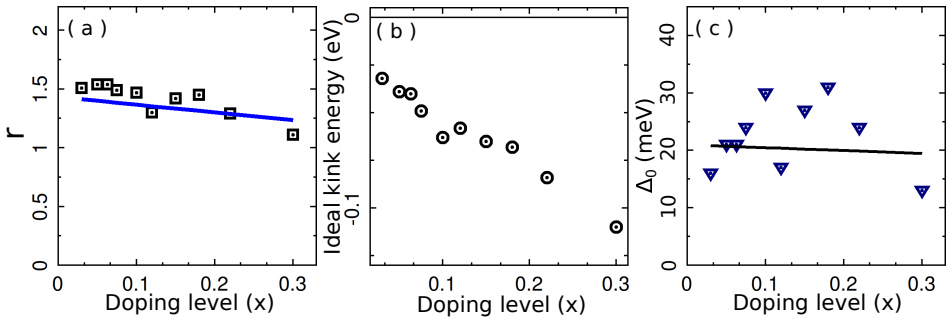

Figure 3.4: (a) The ratio of low and high velocities, r, as a function of doping levels, and (b) ideal kink energy, (c) ECFL energy parameter Δ_0 as a function of doping levels for LSCO data in the main text.

3.6 Bi2201 above Tc data

In this section, we present our ARPES kink analysis for OD Bi2201 above Tc using data available in Ref. ([42]). ARPES kinks in the single-layer compounds Bi2201, as also LSCO, are observed to have weak to moderate temperature dependence. Therefore, even though our data in Fig. (3.5) is for T above Tc, the temperature variable

Γ_0 appears to be quite small. In Fig. (3.5), we predict the EDC dispersions for OD Bi2201 data using Eq. (3.2) for measured experimental MDC variables in Table (3.4).

MDCs						EDCs			
Bi2201 above Tc ARPES data				E_{kink}^{MDC}(meV)		E_{kink}^{EDC}(meV)		V_H^* (eV Å)	
x (doping level)	V_L (eV Å)	V_H (eV Å)	$\hat{k}_{kink}$ ($Å^{-1}$)	Calculated	Measured	Calculated	Measured	Calculated	Measured
0.225	1.7 ± 0.1	4.5 ± 0.4	-0.039 ± 0.005	75 ± 28	76 ± 5	72 ± 28		3.24 ± 0.80	
0.24	1.9 ± 0.1	4.9 ± 0.3	-0.033 ± 0.005	82 ± 21	80 ± 5	77 ± 21		3.58 ± 0.60	
0.252	2.0 ± 0.2	4.2 ± 0.2	-0.035 ± 0.005	78 ± 16	74 ± 5	75 ± 16		3.42 ± 0.39	
0.258	1.7 ± 0.2	4.1 ± 0.2	-0.039 ± 0.005	80 ± 17	77 ± 5	75 ± 17		3.11 ± 0.40	
0.27	1.8 ± 0.1	4.0 ± 0.3	-0.039 ± 0.005	79 ± 22	79 ± 5	76 ± 22		3.17 ± 0.56	

Table 3.4: ARPES kink analysis for various OD Bi2201 above Tc [42] in Fig.3.5. We measured all $\Gamma_0 \lesssim 10$ meV. The uncertainties for the calculated kink energies were determined by error propagation, and the uncertainties for the experimental variables were given by half of the instrumental resolution.

Our analysis suggests $V_H^* < V_H$ as in Bi2212 and LSCO. Kink energies for MDCs were estimated theoretically, and compared with the experimental values in Table (3.4), suggesting our data analysis is reliable. We find that the ratio $V_H/V_H^* \sim 1.37 - 1.4$ is consistently larger than in the other two families and should be easy to measure. Further high resolution EDC data at different doping is needed to check the predictions of the present analysis.

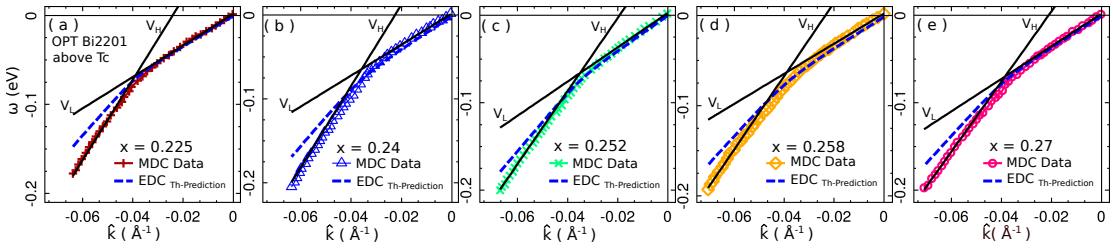

Figure 3.5: ARPES kinks data for various OD Bi2201 compounds above Tc [42] compared to theoretical ECFL curves (solid lines) using parameters in Table (3.4). From (a) to (e) the doping level varies between $0.225 < x < 0.27$, and the blue dashed line is the theoretically predicted EDC spectrum using Eq. (3.2). We estimated all $\Gamma_0 \lesssim 10$ meV.

3.7 Electron-Boson coupling theory of kinks

The electron Boson mechanism suggested in Ref. ([70]) and others [33, 46], is the coupling of the electrons to Bosonic modes (such as phonons), located at the kink energy. To illustrate the basic idea, we first consider free electrons coupled to an Einstein phonon mode of energy $\omega_0 = .08$ eV [33, 46], with coupling constant g. In this case, the spectral function is expressed in terms of a momentum independent self-energy $\Sigma(\omega)$, as

$$A(\vec{k},\omega) = -\frac{1}{\pi}\frac{\mathrm{Im}\, m\Sigma(\omega)}{(\omega - \xi_k - \Re e\Sigma(\omega))^2 + (\mathrm{Im}\, m\Sigma(\omega))^2}, \tag{3.13}$$

where $\xi_k \equiv \varepsilon_k - \mu$, ε_k is the bare dispersion, and μ is the chemical potential. The real and imaginary parts of the self-energy due to the electron-phonon interactions are given by the well known formulas: [71, 72]

$$\begin{aligned} \mathrm{Im}\, m\Sigma(\omega) &= -\pi g^2 \sum_{\pm} N(\omega + \mu \pm \omega_0) \times \\ &\quad \left[f^{\mp}(\omega \pm \omega_0) + n(\omega_0) \right], \\ \Re e\Sigma(\omega) &= -\frac{1}{\pi} \int d\nu \frac{\mathrm{Im}\, m\Sigma(\nu)}{\omega - \nu}, \end{aligned} \tag{3.14}$$

where $f^-(\nu) \equiv f(\nu)$, $f^+(\nu) \equiv \bar{f}(\nu) \equiv 1 - f(\nu)$, $f(\nu)$ and $n(\nu)$ are the Fermi and Bose distribution functions respectively, and $N(E) \equiv \frac{1}{N_s} \sum_k \delta(E - \varepsilon_k)$ is the local density of states for the free electrons. Since the relevant frequency range for the self-energy is $|\omega| \sim \omega_0$, and $\omega_0 \ll W$, where W is the bandwidth, we neglect the frequency dependence in the density of states, i.e. $N(\omega + \mu \pm \omega_0) \approx N(\mu) \approx N(\varepsilon_f)$, where ε_f is the Fermi energy. Furthermore, the strength of the electron-phonon coupling is given by the dimensionless parameter [73] $\lambda \equiv \frac{2N(\varepsilon_f)g^2}{\omega_0}$. Therefore, the imaginary part of the self-energy is expressed directly in terms of λ as

$$\mathrm{Im}\, m\Sigma(\omega) = -\frac{\pi\lambda\omega_0}{2} \sum_{\pm} \left[f^{\mp}(\omega \pm \omega_0) + n(\omega_0) \right]. \tag{3.15}$$

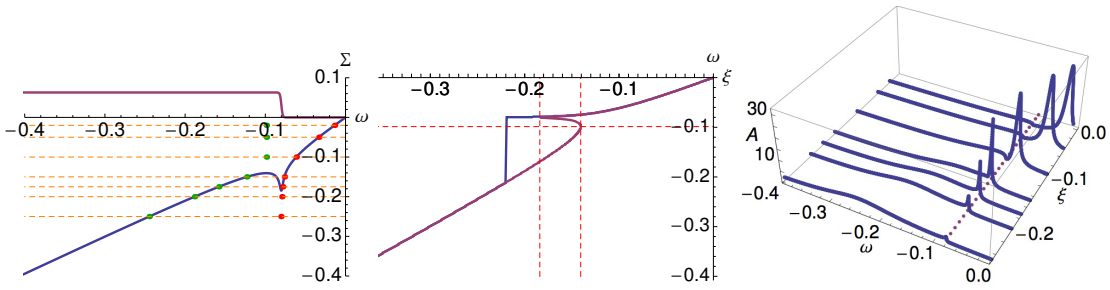

Figure 3.6: Results for free electrons coupled to an Einstein phonon mode of frequency $\omega_0 = .08$ eV, with coupling strength $\lambda = 0.5$, at $T = 10$ K. **Right** panel: The EDCs at several representative momenta, the variable $\xi = v_f(k - k_F) = (1 + \lambda)V_L(k - k_F)$ here and in later figures. The dashed line indicates the phonon frequency, $\omega = -\omega_0$. Each EDC has two well-defined features, a peak followed by a hump (separated by a sharp dip for low momentum EDCs). **Middle** panel: The MDC dispersion (magenta) has no jump while the EDC dispersion (blue) shows a jump. The two vertical dashed lines partition momentum space into three regions. The horizontal dashed line indicates the location of the hump in the EDCs in the first (low-momentum) region. In the first two regions, the EDC dispersion follows the MDC dispersion (closest to zero frequency), while in the third (high momentum) region, it stays pinned to the phonon frequency over a large range of momentum, until it discontinuously jumps back down to the MDC dispersion. Note that $V_H = V_H^*$. **Left** panel: $\omega - \Re e\Sigma(\omega)$ and $-\mathrm{Im}\, m\Sigma(\omega)$ vs. ω. The horizontal dashed lines indicate the momenta associated with the corresponding EDCs in the right panel. The red dots indicate the locations of the peaks, and the green dots indicate the locations of the humps, as determined directly from each EDC.

We initially choose a typical intermediate strength value of $\lambda = 0.5$. We also add a small broadening $\eta = .01$ eV to the imaginary part of the self-energy. In Fig. (3.6), we display $\omega - \Re e\Sigma(\omega)$ and $-\mathrm{Im}\, m\Sigma(\omega)$ vs. ω (left panel), the EDC and MDC dispersions (middle panel), as well as the EDCs at several representative momenta (right panel) at $T = 10$ K. The EDC and MDC dispersions as well as the EDCs can be understood directly from the real and imaginary parts of the self-energy using Eq. (3.13). From Eq. (3.13), the the MDC at fixed ω is a Lorentzian of width $-\mathrm{Im}\, m\Sigma(\omega)$ and peak position $\xi^*(\omega) = \omega - \Re e\Sigma(\omega)$ [70]. Therefore, the MDC dispersion is obtained by inverting $\xi^*(\omega)$ to obtain $E(\xi)$. Since $\omega - \Re e\Sigma(\omega)$ is not one-to-one, $E(\xi)$ is a multi-valued function.

To understand the EDC dispersion, we first examine the EDC curves in the right panel of Fig. (3.6). The momentum ξ associated with each curve is given by the location of the corresponding horizontal dashed line along the vertical axis in the left panel. The EDC at each momentum has two distinguishable features, a peak followed by a hump. In the left panel, the red and green dots indicate the location of the peak and hump, respectively, at each momentum, as determined directly from the EDC.

We partition the EDCs into three distinct momentum regions, $|\xi| < |\xi_1|$, $|\xi_1| < |\xi| < |\xi_2|$, and $|\xi| > |\xi_2|$, where the momenta ξ_1 and ξ_2 (the low-energy kink momentum) are denoted by the dashed vertical lines in the middle panel of Fig. (3.6). In the first region, $|\xi| < |\xi_1|$, the peak location, E_p^*, disperses according to the equation $\xi = E_p^* - \Re e\Sigma(E_p^*)$, while the hump location, E_h^*, remains at a fixed frequency, displayed by the horizontal dashed line in the middle panel. In addition, there is a sharp dip

between the peak and the hump which is pinned to the phonon frequency, $-\omega_0$. Since $\mathrm{Im}\, m\Sigma(E_p^*)$ is constant throughout this region, the height of the peak does not change. On the other hand, since $|E_h^* - \xi - \Re e\Sigma(E_h^*)|$ decreases as $|\xi|$ is increased (and of course $\mathrm{Im}\, m\Sigma(E_h^*)$ is constant), the hump height grows as $|\xi|$ approaches $|\xi_1|$. Nevertheless, since the peak height remains greater than the hump height throughout this region (as will be shown below), the EDC dispersion is given by $E^* = E_p^*$.

In the second region, $|\xi_1| < |\xi| < |\xi_2|$, both E_p^* and E_h^* disperse according to the equation $\xi = E_{p,h}^* - \Re e\Sigma(E_{p,h}^*)$, E_p^* being the root closest to, and E_h^* being the root farthest from, zero frequency. Since $\mathrm{Im}\, m\Sigma(E_p^*)$ continues to remain constant and has the same value as in the first region, so does the height of the peak. Moreover, since $\mathrm{Im}\, m\Sigma(E_h^*)$ remains constant as well, the height of the hump remains the one which it reached at $\xi = \xi_1$. Finally, since $|\mathrm{Im}\, m\Sigma(E_h^*)| > |\mathrm{Im}\, m\Sigma(E_p^*)|$, the peak height is greater than the hump height, and therefore $E^* = E_p^*$.

In the third region, $|\xi| > |\xi_2|$, E_p^* is pinned to the phonon frequency $-\omega_0$, while E_h^* continues to disperse according to the equation $\xi = E_h^* - \Re e\Sigma(E_h^*)$. Since $\mathrm{Im}\, m\Sigma(E_h^*)$ continues to have the same value as in the second region, so does the height of the hump. Meanwhile, the peak height decreases, since $|E_p^* - \xi - \Re e\Sigma(E_p^*)|$ increases as $|\xi|$ is increased. Although initially $E^* = E_p^* = -\omega_0$, eventually, after $|\xi|$ has been sufficiently increased, the peak height falls below the hump height, and $E^* = E_h^*$. Accordingly, in the middle panel, we see that in first two regions, the EDC dispersion follows the MDC dispersion, $E^* = E$ (closest to zero frequency). However, in the third region, E^* stays fixed at $-\omega_0$, until at sufficiently high momentum, it jumps

back down to the MDC dispersion. Since the MDC and EDC dispersions coincide for large momentum, the velocities V_H and V_H^* are equal. We take these three features, a discontinuous jump in the EDC dispersion, a peak pinned to the phonon frequency in the EDC over a prolonged range of momentum, and the equality $V_H = V_H^*$, to be signatures of electron-Boson coupling in ARPES experiments. Similar calculations to the one above can be found in [70, 33], with analogous results.

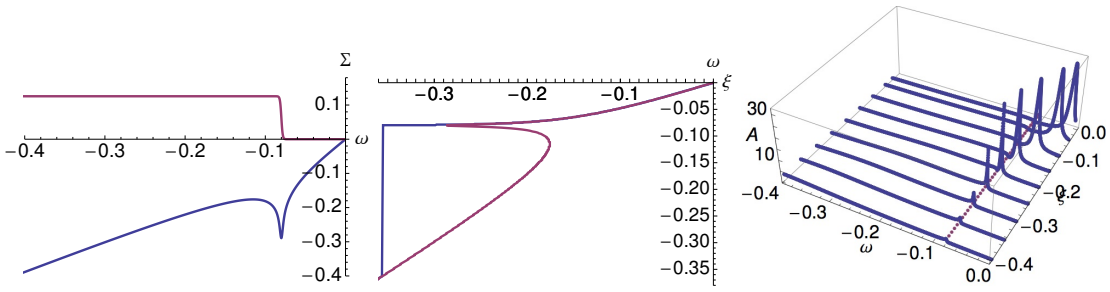

Figure 3.7: To explore the effects of raising λ, we set $\lambda = 1$ while leaving all other parameters unchanged from Fig. (3.6). As a result, the kink momentum in the MDC dispersion becomes bigger, the hump in the EDCs is suppressed, the EDC dispersion stays pinned to the phonon frequency over a larger range of momentum, and the magnitude of the jump in the EDC dispersion grows.

To examine the effects of raising λ, we set $\lambda = 1$ leaving all other parameters unchanged, and plot the corresponding results in Fig. (3.7). This causes several noticeable changes to the results in Fig. (3.6). 1) The kink in the real part of the self-energy becomes sharper, which leads to a larger kink momentum, ξ_2, in the MDC dispersion. 2) $-\mathrm{Im}\, m\Sigma(E_h^*)$ becomes bigger, causing the height of the hump to go down. 3) As a direct consequence of 2), the range over which the EDC dispersion stays pinned to the phonon frequency becomes more prolonged in momentum space, and therefore the

magnitude of the jump in the EDC dispersion also becomes bigger.

Setting $T \to 0$ in Eq. (3.15), and plugging it into Eq. (3.14), we find that to linear order in $\omega \ll \omega_0$, $\Re e\Sigma(\omega) = -\lambda\,\omega$. Therefore, $\lambda = \frac{v_f}{V_L} - 1$ (see also [74]). According to the normal state data ($T = 115$ K) from [31, 46, 75] (since $T \ll \omega_0$, this zero temperature formula still applies), $V_L = 1.47\text{eV}\,\mathring{A}$ and $v_f = 2.7\text{eV}\,\mathring{A}$, yielding $\lambda = 0.84$. In principle, one might argue for the larger value of $v_f \sim 5.4$ eV $\mathring{A}$ from the ARPES observed width of the band [2], leading to $\lambda \sim 2.67$, a very high value indeed. However, we will assume, with several authors of the Boson-coupling models, that the smaller estimate is overall more reasonable. Using these experimentally relevant values, in Fig. (3.8), we plot $\omega - \Re e\Sigma(\omega)$ and $-\text{Im}\, m\Sigma(\omega)$ vs. ω (left panel), as well as the MDC and EDC dispersions (middle panel), and the EDCs at several representative momenta (right panel). Due to the higher value of T, the self-energy curves have been rounded out somewhat as compared to Fig. (3.6), but retain the same features. We see that the EDC dispersion once again follows the MDC dispersion (closest to zero frequency) in the first two momentum regions, until it (nearly) flattens out in the third region, where the peak is pinned to the phonon frequency, $-\omega_0$, in the corresponding EDCs. As the momentum is increased such that the height of this peak shrinks below the height of the hump, the EDC dispersion jumps discontinuously down from the phonon frequency, to the MDC dispersion. Consequently, we see that the velocities of the MDC and EDC dispersion coincide above the kink; i.e. $V_H = V_H^*$.

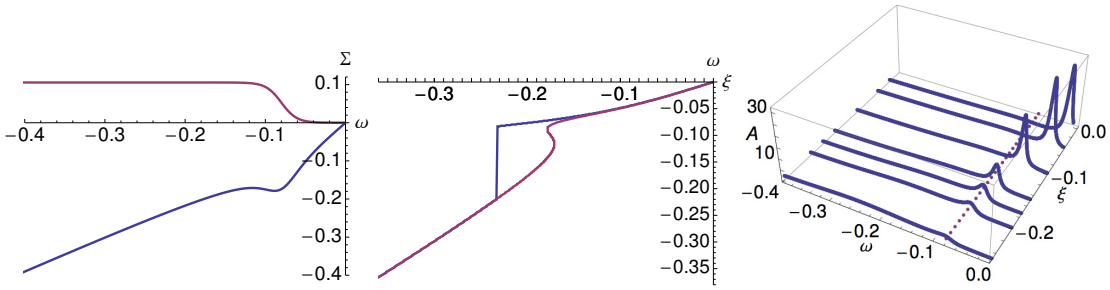

Figure 3.8: We now use the experimentally relevant values of $\lambda = 0.84$ and $T = 115$ K. The curves retain the same qualitative features as in Fig. (3.6), which are less sharp in the present case due to the higher value of T.

We now examine how these results are affected by retaining the full frequency-dependence of the density of states in Eq. (3.14). Just as was done in [46], we use the dispersion tb2 from [75]. In this case, $\varepsilon_f = 0$ and $N(\varepsilon_f) = 0.61$ eV^{-1}. Retaining the same values of $T = 115$ K and $\lambda = 0.84$, we set $g = 0.23$ eV in Eq. (3.14). We also set $\mu \approx \varepsilon_f = 0$. In Fig. (3.9), we plot $\omega - \Re e\Sigma(\omega)$ and $-\mathrm{Im}\, m\Sigma(\omega)$ vs. ω (left panel), as well as the MDC and EDC dispersions (middle panel), and the EDCs at several representative momenta (right panel). Due to the functional form of the density of states (see the inset of the left panel), the MDC dispersion acquires two additional branches which yield large frequency values. In the first two momentum regions (below the low-energy kink momentum), the EDC dispersion follows the lowest-frequency branch of the MDC dispersion. As the momentum increases into the third region (above the low-energy kink momentum), the peak stays pinned to the phonon frequency in the corresponding EDCs. Moreover, since $|\mathrm{Im}\, m\Sigma\left(E(\xi)\right)| \gg |\mathrm{Im}\, m\Sigma(-\omega_0)|$, where $E(\xi)$ can be any branch of the MDC dispersion, the EDC dispersion stays pinned to the

phonon frequency as well. As the momentum is increased further and the height of the peak decreases sufficiently, the EDC dispersion jumps discontinuously onto the highest-frequency branch of the MDC dispersion, since this is the one with the smallest value of $|\mathrm{Im}\, m\Sigma\,(E(\xi))\,|$, and hence $V_H = V_H^*$. This small value of $|\mathrm{Im}\, m\Sigma\,(E(\xi))\,|$ leads to a noticeable hump at high-frequencies in the corresponding EDCs.

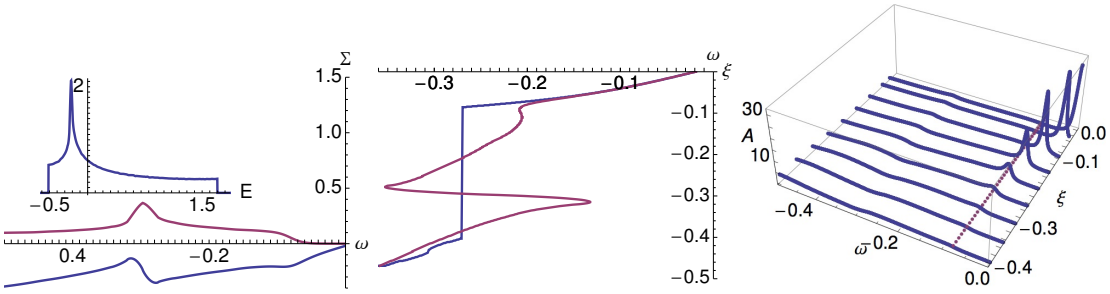

Figure 3.9: We explore the effects of using the full frequency-dependence of the density of states in Eq. (3.14), with $\lambda = 0.84$ and $T = 115$ K. Due to the functional form of the density of states (displayed as an inset in the left panel), the MDC dispersion acquires two additional branches which yield large frequency values. Below the low-energy kink momentum, the EDC dispersion follows the lowest-frequency branch of the MDC dispersion. Above the low-energy kink momentum, the EDC dispersion initially stays pinned to the phonon frequency, until it discontinuously jumps onto the highest-frequency branch of the MDC dispersion ($V_H = V_H^*$). A noticeable hump also develops at high-frequencies, in the corresponding EDCs.

Thus far, we have considered only free electrons coupled to a Boson mode. We now include electron-electron correlations. Following [25], we assume that

$$\mathrm{Im}\, m\Sigma_{el-el}(\omega) = -\frac{(\tau^2+\omega^2)}{\Omega_0}\exp\left[\frac{-(\tau^2+\omega^2)}{\nu_0^2}\right] - \eta, \tag{3.16}$$

where $\Sigma_{el-el}(\omega)$ is the self-energy due only to electron-electron correlations, $\tau \equiv \pi k_B T$, $T = 115$ K, $\Omega_0 = .14$ eV, $\nu_0 = .5$ eV, and we set $\eta = .01$ eV. This phenomenological form for $\mathrm{Im}\, m\Sigma_{el-el}(\omega)$ reproduces the correct Fermi-liquid behavior at low frequencies, and extrapolates to high frequencies in a reasonable way. Furthermore, we assume a flat band for ε_k of bandwidth W, i.e $N(E) = \frac{1}{W}\Theta(\frac{W}{2} - |E|)$, and set $\mu \approx \varepsilon_f = 0$. Retaining the same values of $N(\varepsilon_f) = 0.61$ eV^{-1} and $\lambda = 0.84$ as before, yields the values $W = 1.64$ eV and $g = 0.23$ eV. The self-energy is now given by the sum $\Sigma(\omega) = \Sigma_{el-el}(\omega) + \Sigma_{el-ph}(\omega)$, where the imaginary part of the latter term is

$$\begin{aligned} \mathrm{Im}\, m\Sigma_{\text{el-ph}}(\omega) &= -\pi g^2 \sum_{\pm} A_{\text{el-el,loc}}(\omega \pm \omega_0) \times \\ &\quad \left[f^{\mp}(\omega \pm \omega_0) + n(\omega_0) \right], \end{aligned} \tag{3.17}$$

while the real part is as usual given by applying the Hilbert transform to Eq. (3.17). Here, $A_{\text{el-el,loc}}(\omega) = \frac{1}{N_s}\sum_k A_{\text{el-el}}(\vec{k}, \omega)$, where $A_{\text{el-el}}(\vec{k}, \omega)$ is given by Eq. (3.13) with the substitution $\Sigma(\omega) \to \Sigma_{\text{el-el}}(\omega)$. Eq. (3.13) continues to express $A(\vec{k}, \omega)$ in terms of $\Sigma(\vec{k}, \omega)$, where both objects now include electron-electron and electron-phonon correlations.

In Fig. (3.10), we plot $\omega - \Re e\Sigma(\omega)$ and $-\mathrm{Im}\, m\Sigma(\omega)$ vs. ω (left panel), as well as the MDC and EDC dispersions (middle panel), and the EDCs at several representative momenta (right panel), from this calculation. Due to the specific form of the self-energy, $\Sigma_{el-el}(\omega)$ (both $-\mathrm{Im}\, m\Sigma_{el-el}(\omega)$ and $A_{\text{el-el,loc}}(\omega)$ are displayed as an inset in the left panel), the highest-frequency branch of the MDC dispersion yields very large

values of the frequency. Just as in the cases considered above, for momentum $|\xi|$ below the low-energy kink momentum, the EDC dispersion follows the lowest-frequency branch of the MDC dispersion, $E_l(\xi)$. As the momentum $|\xi|$ is increased above the low-energy kink momentum, the rapid increase in $|\mathrm{Im}\, m\Sigma\,(E_l(\xi))\,|$ causes the peak in the EDC as well as the EDC dispersion to stay pinned to the phonon frequency. As the momentum is increased further, $|\mathrm{Im}\, m\Sigma\,(E_h(\xi))\,|$ becomes comparable to $|\mathrm{Im}\, m\Sigma(-\omega_0)|$, where $E_h(\xi)$ is the highest-frequency branch of the MDC dispersion. At this point, the EDC dispersion jumps discontinuously from the phonon frequency onto the highest-frequency branch of the MDC dispersion, and hence $V_H = V_H^*$. This is also reflected in the corresponding EDCs, which acquire a hump at high-frequencies.

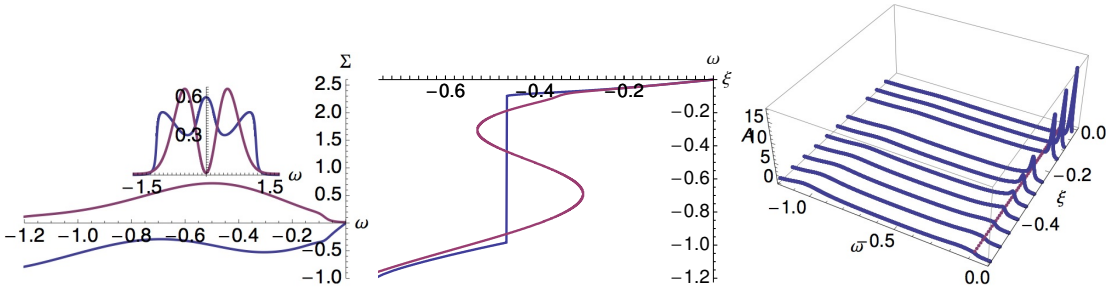

Figure 3.10: We explore the effects of Fermi-liquid-like electron-electron correlations (Eq. (3.16)), with $\lambda = 0.84$ and $T = 115$ K. Due to the functional form of the self-energy, $\Sigma_{el-el}(\omega)$ (both $-\mathrm{Im}\, m\Sigma_{el-el}(\omega)$ and $A_{\text{el-el,loc}}(\omega)$ are displayed as an inset in the left panel), the highest-frequency branch of the MDC dispersion yields very large values of the frequency. Below the low-energy kink momentum, the EDC dispersion follows the lowest-frequency branch of the MDC dispersion. Above the low-energy kink momentum, the EDC dispersion initially stays pinned to the phonon frequency, until it discontinuously jumps onto the highest-frequency branch of the MDC dispersion ($V_H = V_H^*$). This is also reflected in the corresponding EDCs, which acquire a hump at high-frequencies.

In conclusion, we find that in all of the above cases of electrons interacting

with a Boson mode, the EDCs are characterized by three signatures: (1) a peak pinned to the Boson-frequency over a large range of momentum, (2) the EDC dispersion jumps discontinuously from the Boson-frequency onto (the highest-frequency branch of) the MDC dispersion, and (3) $V_H = V_H^*$. These three features are jointly present for most parameters explored, and may be viewed as the signatures of kinks produced by this mechanism.

3.8 Extremely Correlated Fermi liquid theory of kinks

In this section we present the theoretical details of the ECFL calculation of kinks. We first show the results of a low energy and momentum expansion of the ECFL Greens function in terms of a few parameters. Earlier studies [23, 76, 16] show that the two self energies Φ, Ψ of the ECFL theory are to a large extent similar to the self energies of a standard intermediate coupling Fermi liquid, and yet due to their specific combination that occurs in Eq. (3.18) and Eq. (3.20) end up providing a non trivial resulting theory. Indeed in Ref. ([23]) a similar low energy expansion in high dimensions, was tested successfully against the numerical results of the Dynamical Mean Field Theory (DMFT). It should be noted that the DMFT theory is designed for high dimensions, where the momentum dependence of the Dyson self energy and Ψ self energy of the ECFL theory drops out. In this section we allow for momentum dependence of both self energies in the ECFL formalism, this is in-fact the only distinction between the present expansion and that in Ref. ([23]). We see below that this momentum

dependence is essential for describing the low energy kinks in the occupied part of the ARPES spectrum.

3.8.1 Low energy expansion of the ECFL theory

We start with the ECFL Greens function $\mathcal{G}$ expressed in terms of the auxiliary Greens function $\mathbf{g}$ and the caparison function $\widetilde{\mu}$ Ref. ([1]) and Ref. ([34]), we write

$$\mathcal{G}(\vec{k}, i\omega) = \mathbf{g}(\vec{k}, i\omega) \times \widetilde{\mu}(\vec{k}, i\omega), \tag{3.18}$$

and with the latter expressed in terms of the two self energies $\Phi(\vec{k}, i\omega_n), \Psi(\vec{k}, i\omega_n)$ as:

$$\widetilde{\mu}(\vec{k}, i\omega_n) = 1 - \frac{n}{2} + \Psi(\vec{k}, i\omega_n) \tag{3.19}$$

$$\mathbf{g}^{-1}(\vec{k}, i\omega_n) = i\omega_n + \boldsymbol{\mu} - (1 - \frac{n}{2})\varepsilon_k - \Phi(\vec{k}, i\omega_n), \tag{3.20}$$

where n is the electron number per site, $\omega_n = (2n+1)\pi/\beta$ the Matsubara frequency, which we analytically continue $i\omega \to \omega + i0^+$. Let us define $\hat{k}$ as the *normal deviation* from the Fermi surface i.e. $\hat{k} = (\vec{k} - \vec{k}_F).\vec{\nabla}\varepsilon_{k_F}/|\vec{\nabla}\varepsilon_{k_F}|$. Our first objective is to Taylor expand these equations for small ω and $\hat{k}$, as explained above. We carry out a low

frequency expansion as follows:

$$1 - \frac{n}{2} + \Psi(\vec{k}, \omega) \quad = \quad \alpha_0 + c_\Psi(\omega + \nu_\Psi \ \hat{k}\, v_f) + i\mathcal{R}/\gamma_\Psi + \mathcal{O}(\omega^3), \tag{3.21}$$

where the frequently occurring Fermi liquid function $\mathcal{R} = \pi\{\omega^2 + (\pi k_B T)^2\}$, $v_f = (\partial_k \varepsilon_k)_{k_F}$ is the *bare* Fermi velocity, and the four parameters $\alpha_0, c_\Psi, \nu_\Psi, \gamma_\Psi$ are coefficients in the Taylor expansion having suitable dimensions. Similarly we expand the auxiliary Greens function

$$\mathbf{g}^{-1}(k, \omega) = (1 + c_\Phi)\left(\omega - \nu_\Phi \ \hat{k}\, v_f + i\mathcal{R}/\Omega_\Phi + \mathcal{O}(\omega^3)\right), \tag{3.22}$$

where we have added another three coefficients in the Taylor expansion $c_\Phi, \nu_\Phi, \Omega_\Phi$.

To carry out this reduction we first trade the two parameters c_Ψ, γ_Ψ in favor of parameters Ω_Ψ and s by defining $c_\Psi = \frac{\alpha_0}{\Omega_\Psi}$ and $\gamma_\Psi = \frac{s\Omega_\Phi}{c_\Psi}$, where the dimensionless parameter $0 \leq s \leq 1$. With these expansions and the quasiparticle weight determined in terms of the expansion parameters as $Z = \frac{\alpha_0}{1+c_\Phi}$, we find

$$\mathcal{G} = \frac{Z}{\Omega_\Psi} \frac{\Omega_\Psi + \omega + \nu_\Psi \ \hat{k}\, v_f + i\mathcal{R}/(s\Omega_\Phi)}{\omega - \nu_\Phi \ \hat{k}\, v_f + i\mathcal{R}/\Omega_\Phi}. \tag{3.23}$$

Using $A(\hat{k},\omega) = -\frac{1}{\pi}\mathrm{Im}\, m\, \mathcal{G}$ we find the spectral function

$$A(\hat{k},\omega) \;=\; \frac{Z}{\pi}\frac{\frac{\mathcal{R}}{\Omega_\Phi}}{(\omega - \nu_\Phi\ \hat{k}\, v_f)^2 + (\frac{\mathcal{R}}{\Omega_\Phi})^2} \times \widetilde{\mu}_c(\hat{k},\omega) \tag{3.24}$$

Here the caparison *factor*, (not to be confused with the caparison *function* in Eq. (3.18)), is found as

$$\begin{aligned} \widetilde{\mu}_c(\hat{k},\omega) &= 1 - \xi(\hat{k},\omega) \\ \xi(\hat{k},\omega) &= \frac{1}{\Delta_0}(\omega - \nu_0\ \hat{k}\, v_f) \end{aligned} \tag{3.25}$$

In Eq. (3.25) we have introduced two composite parameters

$$\Delta_0 = \frac{s}{1-s}\Omega_\Psi, \quad \text{and} \quad \nu_0 = \frac{1}{1-s}\nu_\Phi + \frac{s}{1-s}\nu_\Psi. \tag{3.26}$$

This procedure eliminates the *three* old parameters s, Ω_Ψ and ν_Ψ in favor of the *two* emergent energy scale Δ_0 and velocity ν_0.

It is interesting to count the reduction in the number of free parameters from the starting value of seven in Eq. (3.21) and Eq. (3.22). Already in Eq. (3.23) we have a reduction to six, since the quasiparticle weight Z combines two of the original parameters. Since Eq. (3.26) subsumes three parameters into two, the spectral function in Eq. (3.24) contains only five parameters: the two velocities $\nu_0\, v_f, \nu_\Phi\, v_f$, and the two energies Ω_Φ, Δ_0, in addition to the overall scale factor Z.

We will see below that the parameters that are measurable from energy dispersions are best expressed in terms of certain combinations of the velocities. In order to make the connection with the experiments close, we will redefine the two velocities in terms of an important dispersion velocity at the lowest energies V_L and a dimensionless ratio r, on using the definitions:

$$\begin{aligned} \nu_\Phi \, v_f &= V_L \\ \nu_0 \, v_f &= r \times V_L. \end{aligned} \tag{3.27}$$

In order to account for the difference between laser ARPES and synchrotron AREPS having different incident photon energies, we will make two phenomenological modifications in Eq. (3.24) following Ref. ([2])

$$\mathcal{R}(\omega)/\Omega_\Phi \to \mathcal{R}(0)/\Omega_\Phi = \pi\{\pi k_B T\}^2/\Omega_\Phi + \eta \equiv \Gamma_0 \tag{3.28}$$

where η represents an elastic energy from impurity scattering, dependent upon the energy of the incident photon in the ARPES experiments. In the spirit of a low energy expansion $\mathcal{R}$ is evaluated at $\omega = 0$. Thus Γ_0 is a T dependent constant, which subsumes the two parameters η and Ω_Φ, and thus the total parameter count is still five. Secondly for extension to higher energies, we "renormalize" the parameter ξ in Eq. (3.25) according to a recently discussed prescription following from a theoretical calculation Ref. ([35]) as $\widetilde{\mu_c} \to \{1 - \frac{\xi}{\sqrt{1+c_a\xi^2}}\}$, where $c_a \sim 5.4$ near optimum doping $\delta \sim 0.15$ as

estimated recently. This correction ensures that the caparison factor exhibits the correct linear behavior for small ξ, and remains positive definite at high energies. Thus we write the spectral function in terms of the new variables as

$$A(\vec{k},\omega) = \frac{Z}{\pi}\frac{\Gamma_0}{(\omega - V_L\,\hat{k})^2 + \Gamma_0^2} \times \{1 - \frac{\xi}{\sqrt{1 + c_a\xi^2}}\}, \tag{3.29}$$

with $\xi = \frac{1}{\Delta_0}(\omega - r\,V_L\,\hat{k})$. We should keep in mind that these expressions follow from a low energy expansion, and is limited to small $\hat{k}$ and ω, so that the dimensionless variable $|\xi|_{max} \sim \mathcal{O}(1)$. Microscopic calculations of all these parameters is possible in the ECFL theory. One important parameter is the energy scale Δ_0 which is found to be much reduced from the band width, due to extremely strong correlations. A related energy is the effective Fermi liquid temperature scale where the T^2 dependence of the resistivity gives way to a linear dependence. This scale is estimated in the limit of large dimensions from Ref. ([35]) to be as low as 45 K near optimum doping, i.e. much reduced from naive expectations.

For the present purposes we take a different track, we note that the ARPES fits are overdetermined, so that we can determine the few parameters of the low energy theory from a fairly small subset of measurements. The five final (composite) parameters defining the spectral function Eq. (3.29) are $Z, V_L, r, \Delta_0, \Gamma_0$, where $c_a \sim 5.4$. Of these Z is multiplicative, it is only needed for getting the absolute scale of the spectral function, and c_a does not play a significant role near zero energy, it is required only at high

energies. Thus the spectra relevant to EDC and MDC will require only *four* parameters $V_L, r, \Delta_0, \Gamma_0$. These suffice to determine the low energy theory and thus to make a large number of predictions; i.e. implying non trivial relationships amongst observables. Many of the predictions rely only on the overall structure of the theory and not its details.

3.8.2 The EDC and MDC dispersion relations and kinks

Starting from Eq. (3.29), we can compute the energy dispersions for MDC (varying $\hat{k}$ while keeping ω fixed) and the EDC spectra (varying ω while keeping $\hat{k}$ fixed). In terms of a momentum type variable

$$Q(\hat{k}) = \Delta_0 + (r-1)\hat{k}\, V_L \tag{3.30}$$

we can locate the peaks of Eq. (3.29) using elementary calculus since c_a only plays a role at high energies, we set $c_a \to 0$ when performing the extremization and find the MDC dispersion

$$E(k) \;=\; \frac{1}{2-r}\left(\hat{k}\, V_L + \Delta_0 - \sqrt{r(2-r)\,\Gamma_0^2 + Q^2}\right), \tag{3.31}$$

and the EDC dispersion

$$E^*(k) \;=\; \left(r\,\hat{k}\,V_L + \Delta_0 - \sqrt{\Gamma_0^2 + Q^2} \right). \tag{3.32}$$

Using these two dispersions and expanding them in different regimes, we can extract all the parameters of the kinks.

3.8.2.1 Kink momentum

As explained in the main paper, when we set $T = 0 = \eta$ so that $\Gamma_0 = 0$, both the EDC and MDC dispersions contain an ideal kink at the kink momentum. Therefore, using Eqs. (3.31) and (3.32), the condition $Q = 0$ locates the kink momentum for both dispersions:

$$\hat{k}_{kink} = \frac{\Delta_0}{(1-r)V_L}, \tag{3.33}$$

it corresponds to occupied momenta, i.e. $\hat{k}_{kink} v_f < 0$, provided that $r > 1$. We thus can express $\Delta_0 = \hat{k}_{kink}\, V_L(1-r)$, enabling us to usefully rewrite

$$Q = (r-1)\, V_L\, (\hat{k} - \hat{k}_{kink}) = \Delta_0 \{1 - \frac{\hat{k}}{\hat{k}_{kink}}\}. \tag{3.34}$$

As required by the ideal kink, Q changes sign at the kink momentum,

$$\text{sign}(Q) = \text{sign}(\hat{k} - \hat{k}_{kink}). \tag{3.35}$$

3.8.2.2 Ideal Kink energies: T=0

Using Eq. (3.31) and Eq. (3.32), in conjunction with Eq. (3.33), the ideal kink energy is the same for both dispersions, and is given by

$$E_{kink}^{ideal} = -\frac{1}{r-1}\Delta_0. \tag{3.36}$$

We can also usefully estimate this ideal kink energy from the asymptotic velocities in the far zone, as explained in the main paper.

3.8.2.3 The non-ideal i.e. $T > 0$ kink energy

The EDC and MDC kink energies for the non-ideal case can be viewed in a couple of ways. We have argued in the main paper that these are best defined by fixing the momentum $\hat{k} = \hat{k}_{kink}$ and reading off the energy at this value. This is an unambiguous method independent of the detailed shape of the kink, since it only requires knowledge of $\hat{k}_{kink}$, which can be found from an asymptotic measurement as we have argued in the main paper. We can put $Q = 0$ and $\hat{k} \to \hat{k}_{kink}$ in Eq. (3.32) and Eq. (3.31) and read off the kink energies:

$$E_{kink}^{EDC} = E_{kink}^{ideal} - \Gamma_0, \tag{3.37}$$

$$E_{kink}^{MDC} = E_{kink}^{ideal} - \Gamma_0\sqrt{\frac{r}{2-r}}. \tag{3.38}$$

We observe that the MDC kink energy is real provided $2 \geq r \geq 1$. Note also that at $T = 0$ and $\eta = 0$, the two energies both reduce to the ideal kink energy.

3.8.2.4 The ideal energy dispersions

At $T = 0$ or for for $|Q| \gg \Gamma_0$, the two dispersions Eq. (3.32) and Eq. (3.31) become:

$$E^*(k) \sim \left[r - (r-1)\,\mathrm{sign}(\hat{k} - \hat{k}_{kink})\right] \hat{k}\, V_L \;+\; 2\Delta_0 \Theta(\hat{k}_{kink} - \hat{k}) \tag{3.39}$$

and

$$E(k) \sim \frac{1}{2-r}\left[1 - (r-1)\,\mathrm{sign}(\hat{k} - \hat{k}_{kink})\right] \hat{k}\, V_L \;+\; \frac{2\Delta_0}{2-r}\Theta(\hat{k}_{kink} - \hat{k}). \tag{3.40}$$

The velocities in the asymptotic regime $|\hat{k}| \gg \hat{k}_{kink}$ can be found from the slopes of these, and are therefore temperature-independent. For $\hat{k} \gg \hat{k}_{kink}$ we get the "low" velocities

$$\begin{aligned} \frac{dE(k)}{d\hat{k}} &= V_L \\ \frac{dE^*(k)}{d\hat{k}} &= V_L^* = V_L \end{aligned} \tag{3.41}$$

and thus the EDC and MDC velocities are identical. For $\hat{k} \ll \hat{k}_{kink}$ we get the "high" velocities

$$V_H = \frac{dE(k)}{d\hat{k}} = \frac{r}{2-r} V_L, \tag{3.42}$$

$$V_H^* = \frac{dE^*(k)}{d\hat{k}} = (2r-1)V_L. \tag{3.43}$$

We may cast Eq. (3.43) into an interesting form

$$V_H^* = \left\{ \frac{3V_H - V_L}{V_H + V_L} \right\} V_L, \tag{3.44}$$

it is significant since the EDC spectrum velocity is exactly determined in terms of the two MDC spectrum velocities. It is also a testable result, we show elsewhere in the paper how this compares with known data. Note that the four independent parameters $V_L, r, \Delta_0, \Gamma_0$ alluded to in the discussion below Eq. (3.29), can be determined from the directly measurable parameters $V_L, V_H, \hat{k}_{kink}, \Gamma_0$ (3.42,3.33,3.11). Therefore, either set of parameters gives complete knowledge of the EDC and MDC dispersions, as well as the spectral function (up to an overall scale).

3.8.2.5 Near Zone: Corrections to Energy dispersion due to finite T.

In the regime dominated by finite T and effects of η the elastic scattering parameter, we can also perform an expansion in the limit when $|Q| \ll \Gamma_0$, using Eq. (3.31)

and Eq. (3.32). The the first few terms are

$$\begin{aligned} E(k) &= \frac{\Delta_0}{1-r} - \sqrt{\frac{r}{2-r}}\,\Gamma_0 + \frac{V_L}{2-r}(\hat{k}-\hat{k}_{kink}) \\ &\quad -\frac{(1-r)^2}{2\sqrt{r(2-r)^3}}\,\frac{V_L^2}{\Gamma_0}(\hat{k}-\hat{k}_{kink})^2 + \ldots \end{aligned} \tag{3.45}$$

Similarly for the EDC dispersion

$$\begin{aligned} E^*(k) &= \frac{\Delta_0}{1-r} - \Gamma_0 + rV_L(\hat{k}-\hat{k}_{kink}) \\ &\quad -\frac{(1-r)^2}{2}\,\frac{V_L^2}{\Gamma_0}(\hat{k}-\hat{k}_{kink})^2 + \ldots \end{aligned} \tag{3.46}$$

These formulas display a shift in the energies due to Γ_0 and also a Γ_0 dependent curvature. Since the regime of this expansion, $|Q| < \Gamma_0$ is different from that of the expansion in Eq. (3.43) and Eq. (3.41), we note that velocities are different as well. Thus one must be careful about specifying the regime for using the velocity formulae.

Let us note that in this regime $|Q| < \Gamma_0$ the two dispersions differ, with the EDC higher.

$$\begin{aligned} E^*(k) - E(k) &= \{\sqrt{\frac{r}{2-r}} - 1\}\Gamma_0 \\ -\frac{(1-r)^2}{2-r}V_L(\hat{k}-\hat{k}_{kink}) &+ \ldots \end{aligned} \tag{3.47}$$

This equation gives a prescription for estimating Γ_0 in cases where the other parameters are known. Alternatively in the MDC dispersion we expect to see a curvature only near

the location of the kink, this is sufficient to fix Γ_0: from Eq. (3.45)

$$\frac{d^2E(k)}{d\hat{k}^2} \;=\; -\frac{(r-1)^2}{\sqrt{r(2-r)^3}}\,\frac{V_L^2}{\Gamma_0}. \tag{3.48}$$

The curvature $\frac{d^2E(k)}{d\hat{k}^2}$ can be estimated from the experimental data to provide an estimate of Γ_0.

3.8.3 The Dyson self energy

For completeness we present the low energy expansion of the Dyson self energy, which gives rise to the spectral function in Eq. (3.29). We may define the Dyson self energy from

$$\Sigma_D \;=\; \omega + \boldsymbol{\mu} - \varepsilon_k - \mathcal{G}^{-1} \tag{3.49}$$

Using Eq. (3.23) we obtain

$$\mathrm{Im}\, m\, \Sigma_D = -\frac{1}{Z}\frac{\mathcal{R}}{\Omega_\Phi}\frac{1-\frac{1}{\Delta_0}(\omega-\nu_0\;\hat{k}\,v_f)}{\{1+(\omega+\nu_\Psi\;\hat{k}\,v_f)/\Omega_\Psi\}^2+\frac{\mathcal{R}^2}{s^2\Omega_\Phi^2\Omega_\Psi^2}} \tag{3.50}$$

The corresponding real part is given by

$$\begin{aligned}
\Re e\,\Sigma_D &= \boldsymbol{\mu} - \boldsymbol{\mu}_0 + \omega - \hat{k}\,v_f \\
&\quad -\frac{1}{Z}\frac{(\omega - \nu_\Phi\ \hat{k}\,v_f) + \frac{1}{\Omega_\Psi}q_2}{\{1 + (\omega + \nu_\Psi\ \hat{k}\,v_f)/\Omega_\Psi\}^2 + \frac{\mathcal{R}^2}{s^2\Omega_\Phi^2\Omega_\Psi^2}} \\
q_2 &= (\omega + \nu_\Psi\ \hat{k}\,v_f)(\omega - \nu_\Phi\ \hat{k}\,v_f) + \frac{\mathcal{R}^2}{s\Omega_\Phi^2}.
\end{aligned} \tag{3.51}$$

The q_2 term is quadratic (or higher) in the small variables $\omega,\ \hat{k}\,v_f$, however these small terms are needed if we want to reproduce exactly Eq. (3.24).

3.8.3.1 Useful identities and some Fermi Liquid parameters.

We list a few useful identities relating the various parameters

$$\begin{aligned}
\Omega_\Psi &= \frac{1-s}{s}\,\Delta_0, \\
s &= \frac{\Delta_0}{\Delta_0 + \Omega_\Psi} \\
\nu_0 &= \frac{\nu_\Phi + s\,\nu_\Psi}{1-s} = r\,\nu_\Phi \\
\nu_\Psi &= \frac{r - 1 - rs}{s}\,\nu_\Phi \\
r - 1 &= \frac{\Delta_0}{\Omega_\Psi}\left(1 + \frac{\nu_\Psi}{\nu_\Phi}\right)
\end{aligned} \tag{3.52}$$

Let us note the Fermi liquid renormalizations from Eq. (3.49)

$$\begin{aligned} \left.\frac{d\Sigma_D}{d\hat{k}}\right|_{FS} &= (\frac{V_L}{Z} - v_f) \\ \left.\frac{d\Sigma_D}{d\omega}\right|_{FS} &= (1 - \frac{1}{Z}) \end{aligned} \tag{3.53}$$

Therefore we write the Fermi liquid mass enhancement that determines the heat capacity as:

$$\frac{m}{m^*} = Z\left\{1 + \frac{1}{v_f}\left.\frac{d\Sigma_D}{d\hat{k}}\right|_{FS}\right\} = V_L/v_f = \nu_\Phi. \tag{3.54}$$

Thus ν_Φ is the inverse mass enhancement factor, obtainable from the ratio of the heat capacity and the bare density of states. In this model we note that ν_Φ is not obliged to vanish as Z near the half filled limit $n \to 1$, but may be a finite number of $O(1)$. This is unlike the Brinkman Rice "heavy metal' type behavior $m/m^* \propto Z$, which is prototypical of theories with a momentum independent self energy.

Finally we note that the condition for the kink to occur is, we recall, $r > 1$. From Eq. (3.52) we see that this requires a finite Ω_Ψ (so that $1 > s > 0$). We also need $\Delta_0 > 0$ and $\left(1 + \frac{\nu_\Psi}{\nu_\Phi}\right) > 0$.

3.9 Conclusion

The main goal of this work is to understand the physical origin of the kinks seen in ARPES studies of a wide class of systems. For this purpose we have listed fifteen systems of topical interest where ARPES kink data is available. Our focus is on the nodal direction data, since the largest volume is available here. We have devised a useful protocol to extract kink parameters from data, where the asymptotic tangents of the kink are used. Using this protocol we have analyzed in detail three families of systems. The main parameters of the kinks are the energy, momentum and the dispersion velocities in EDC and MDC scans, these provide a quantitative data set for testing various theoretical proposals for explaining kinks.

We have next outlined two competing theories of the kinks, and highlighted their distinctive predictions. One is the electron-Boson model, where an Einstein mode of either spin or charge origin couples to the electrons, resulting in a momentum independent self energy. This theory gives rise to kinks in the electron dispersion. The other theory is the strong or extreme correlation theory, where the interactions lead to a momentum dependent self energy in 2 dimensions. This theory also gives rise to kinks in the electron dispersion.

We consider an electron-Boson coupling model and provide detailed calculations of the electron self energy in a Fermi gas and a Fermi liquid with varying electron phonon coupling constants. We next provide details of the origin of kinks using the framework of the extremely correlated Fermi liquid.

While we focussed attention on kinks in the nodal direction in the present work, the ECFL theory is also valid for other directions, it has a momentum dependence in the self energy both normal to the Fermi surface and also along the tangent. The ECFL theory applied to the d-wave superconducting state in the t-J model is expected to lead to further interesting results in the future. For now we note that the observed nodal direction spectra are essentially unchanged at T_c, which makes the nodal direction particularly interesting.

The predictions of the two theories differ significantly and in experimentally testable ways. The Boson-mode theory gives rise to kinks located *at* the energy of the localized mode. The electron Boson coupling can be estimated to be $\lambda \sim 1$ from comparing the bare velocity of the electrons and the renormalized velocity. The bare velocity is obtainable from band theory, while the renormalized velocity can be found from the observed kink momentum and energy. This is quite large when we recall that the largest known elemental coupling in Pb, is $\lambda \sim 1.2$. For the kinks, the Boson-mode theory predicts in Sec. 3.7: (1) a momentum independent peak in the spectral function at the kink energy when $\hat{k} < \hat{k}_{kink}$, (2) a jump in the EDC dispersion at the kink energy but not the MDC dispersion and (3) the EDC and MDC velocities are identical both before and after the kink is crossed.

The extremely strong correlation theory also gives rise to kinks, these originate from the momentum dependence of the self energy in Sec. 3.8. A simple low energy and momentum expansion of the ECFL theory gives inter-relations between observed features of the kinks. It predicts (1) a kink at an emergent low energy scale originating

from Gutzwiller correlations (2) no jump in the EDC dispersion and (3) the EDC velocity is determined by the MDC velocities through Eq. (3.12). It is remarkable that a knowledge of the MDC dispersion suffices to predict the EDC dispersion. The parameters obtained from the MDC also enable us to reconstruct the spectral function at low momentum and energy, in both MDC and EDC scans.

It is thus clear that EDC dispersions hold the key to distinguishing between the two competing theories. EDC dispersion data is sparse but exists, the work on OPT Bi2212 from Ref. ([31]) presents both EDC and MDC dispersions at 115 K. Its resolution is presumably not optimal, since it was an early experiment. Nevertheless we can use it to make a first pass at comparing the two theories. This data set shows that the EDC dispersion is continuous, i.e. has no jump. Further the velocity V_H^* is close to that predicted by the ECFL analysis. The measured spectral function in EDC is rather noisy but does not seem to have a clear immovable feature at E_{kink}. It is roughly fit by the low energy parameterized curves as well, where the MDC is seen to be more symmetric than the EDC cuts.

As noted in Table (3.1) the above case OPT Bi2212 is particularly interesting. Low energy Bosonic modes have been observed in neutron scattering [47, 48], and in momentum resolved electron energy loss experiments [46]. In Ref. ([46]) an MDC dispersion is presented using parameters taken from the Bosonic data. This leads to a rather detailed model, and is shown to provide a reasonable fit to the MDC dispersion and the observed kink, but the EDC dispersion is not available.

The present work also gives the parameters for two other popular systems

LSCO and Bi2201, where we give a set of predictions for the velocities in the EDC dispersion that can be testd in future experiments.

In conclusion we have presented a current summary of the physics of the kinks. We believe that there is urgent need for further high resolution EDC data, and also T dependent scans to explore the rounding of kinks. Using such data one should be able to check the predictions of the theory more thoroughly, and thereby obtain definitive understanding of this important problem of the origin of low energy kinks in ARPES.

Chapter 4

Summary and Concluding remarks

In this dissertation, the novel interpretation of the experimental data of the Angle Resolved Photoemission Spectroscopy (ARPES) experiments has been discussed. The proposed Green's function is the solution to the Gutzwiller projected ground state of t-J Hamiltonian, and it was calculated by "Extremely Correlated Fermi Liquid Theory" (ECFL) by Shastry [1]. The key physics idea of the ECFL theory is contained in "the caparison factor". The caparison factor is an ω dependent adaptive spectral weight that imposes main physics of Gutzwiller projection that works to decrease the spectral weight at high energy while keeping the Fermi surface volume invariance at low energy. The ECFL theory has led to unprecedented success when explaining the ARPES spectra of high Tc cuprate superconductors along the nodal direction. The ECFL theory can fit both laser and synchrotron ARPES spectra of cuprates with only two free variables [2], and the phenomenological ECFL models can fit the ARPES spectra of different cuprate superconductors, optimally doped $Bi_2Sr_2CaCu_2O_{8+\delta}$ and $La_{2-x}Sr_xCuO_4$, as functions

of momentum and energy with the same physical intrinsic parameters [3].

In addition to that, the ECFL theory provides a robust description of the origin of low energy kinks in the ARPES spectra. The low energy bending anomaly, near 50 - 100 meV in energy dispersion, has been observed in the ARPES spectra of high Tc cuprate superconductors and other strongly correlated materials, such as charge density systems, cobaltates, and ferromagnetic iron surfaces. The ARPES kinks present below and above Tc, over the entire doping range from insulator to normal metal in the hole doped phase diagram, and at wide momentum range from nodal to anti-nodal direction. We have investigated two competing theoretical scenarios for the origin of the ARPES kinks. One is the electron-Boson model, and another is the strong correlation model. The theoretical construct of the electron-Boson model is an Einstein mode of either charge or spin coupling to the electrons, leading to the momentum independent Dyson self energy. In the strong correlation model, the interactions evoke a momentum dependent Dyson self energy in two dimensions, and this gives rise to kinks in energy dispersion. The two competing theories have been discussed thoroughly and compared with the available ARPES data, and we showed that the description of correlation kinks is consistent with the ARPES data while the explanation suggested by the electron-Boson model is questionable.

When discussing the correlation description of ARPES kinks, we have demonstrated that the effective protocol of ECFL kink analysis successfully explains the available ARPES kinks data of different cuprate superconductors, Bi2212, LSCO, and Bi2201. The theory depends merely on the two asymptotic tangents of each dispersion

curve (far zone), away from the feature itself (near zone), and this makes it insensitive to the shape of the kink as seen in experiments. The overdetermined calculation uses only four independent parameters to predict sets of many observable relations in the ARPES experiments.

While the ECFL interpretation of the ARPES spectra should be rigorous and addresses comprehensive understanding and definition to the ARPES data, we suggest that our predictions may call for high resolution experiments. For instance, the ARPES data of the EDC energy dispersions of underdoped materials and the asymmetry in the lines shapes of MDCs near the Fermi level, which has been just reported for Hg1201 in Ref. ([58]), would be interesting to investigate when the high resolution experiments are available. In particular, systematic and comprehensive investigation on the property of low energy excitation spectrum of three different single layer cuprate superconductors, Bi2201 LSCO and Hg1201, focusing on concerning the asymmetry in the ARPES line shapes, should be interesting research topic.

Although our discussion in this dissertation focuses on the ARPES spectra along the nodal direction, the theory is valid for other momentum directions. We expect to see further interesting results when the d-wave superconducting state in the t-J model becomes available. For that, we would like to mention the most recent report on progress of the ECFL theory that studies the low energy properties of the infinite dimensional t-J model in Ref. ([35]).

In Fig. (4.1) (from Ref. ([35])), the ECFL theory predicts the resistivity behavior as a function of temperature in infinity dimensions. Recognizing the single particle

Green's function, the exact resistivity of a metal due to inelastic mutual collisions of electrons has been calculated in infinity dimensions. The result in Fig. (4.1) is interesting as we see a clear deviation from the Fermi liquid behavior. Also, we see the resistivity is linearly increasing for temperature greater than $\sim 45\,\mathrm{K}$.

In Fig. (4.2) (from Ref. ([35])), the ECFL result of the chemical potential is plotted as a function of temperature. The chemical potential curves are plotted for different densities, and note that the curve turns around at density between n = 0.6 and 0.7, and the behavior changes at this doping value. Fig. (4.3)(from Ref. ([35])) presents the ECFL calculation of the quasiparticle weight vs. the hole density, δ = 1 - n. In this plot, the quasiparticle weight recedes as δ goes to zero. Comparing to the solid line of numerical quasiparticle weight calculation by DMFT, the nonlinear behavior of the quasiparticle weight vs. δ plot indicates the fluctuations should be beyond the mean field description.

In conclusion, in this dissertation, I have discussed the ECFL theory and its interpretation of the low energy spectrum of strongly correlated matter measured by ARPES. We have shown that the ECFL interpretation of the ARPES spectra is robust and consistent with the available set of experimental data. We should find further interesting discussions when more reports on the high resolution ARPES experiments for various different cuprate superconductors become available.

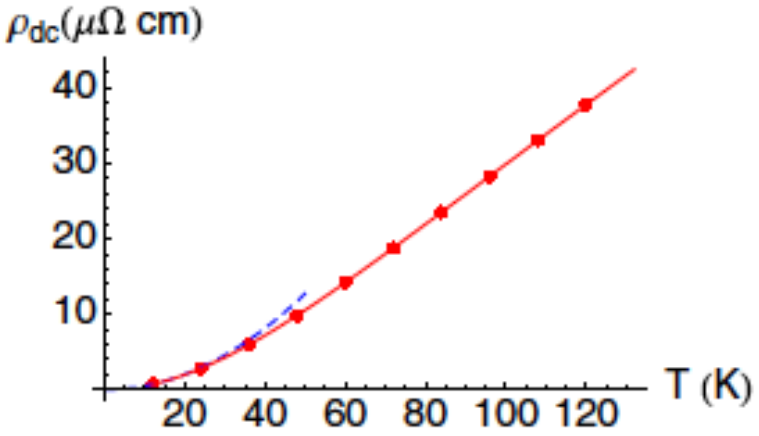

Figure 4.1: ρ_{dc} ($\mu\Omega$ cm) on absolute scale vs T (temperature in Kelvin) for particle density, n = 0.85 (x = 0.15) from Ref. ([35]). The quadratic resistivity of Fermi liquid behavior in the blue dotted line breaks down above $T_{FL} \approx 30$ K, and is followed by a regime of linear resistivity. More information for this plot can be found in Ref. ([35])

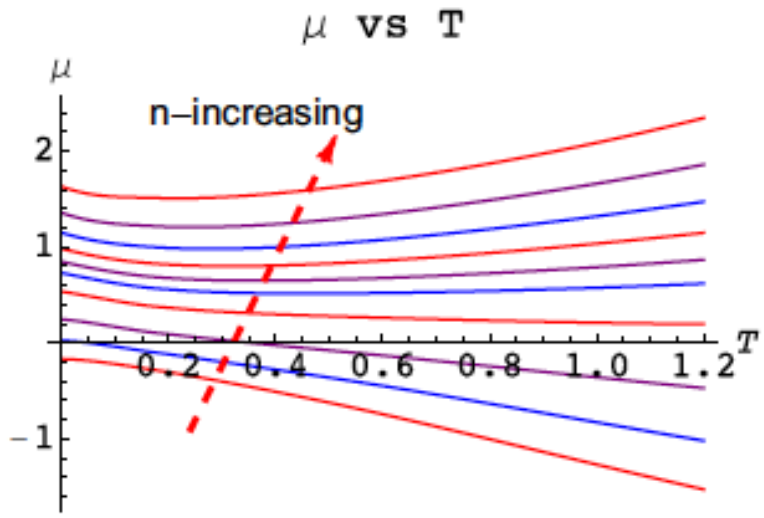

Figure 4.2: Plot of the chemical potential as a function of temperature for various different particle densities, n = 0.4, 0.5, 0.6, 0.7, 0.75, 0.775, 0.8, 0.825, 0.85, 0.875 increasing to the direction of arrow showing. T $\leq$ 1.2. For lower density curves, the chemical potential decreases monotonically as T increasing, and there we see a shallow minimum forms for higher density curves. Note the curve turns around at the particle density of n $\sim$ 0.7. More information for this plot can be found in Ref. ([35])

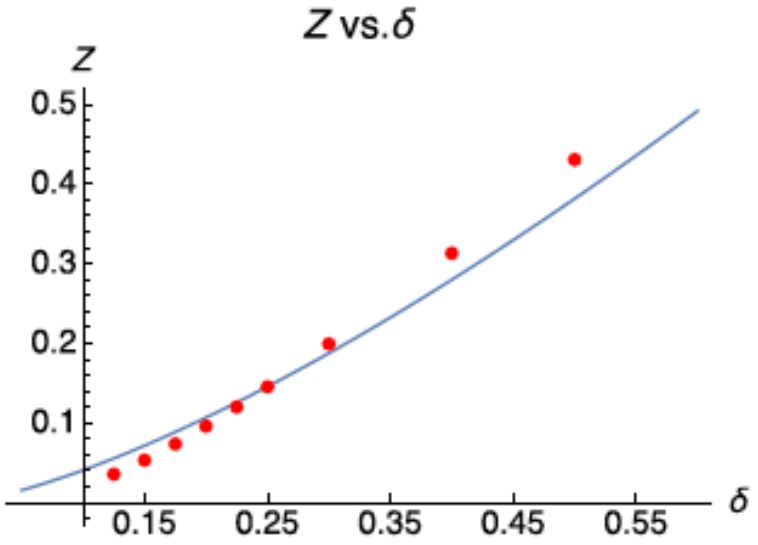

Figure 4.3: The computed quasiparticle weight Z (red dots) vs. the hole density $\delta =$ 1 -n, comparing to the exact numerical results from DMFT [23] that fits very good to the quasiparticle weight formula $\sim \delta^{1.39}$. More information for this plot can be found in Ref. ([35])

Bibliography

[1] Shastry, B. Sriram. Extremely correlated Fermi liquids. *Physical Review letters* **107**.5 (2011): 056403.

[2] Gweon, G-H., B. S. Shastry, and G. D. Gu. Extremely Correlated Fermi-Liquid Description of Normal-State ARPES in Cuprates. *Physical Review Letters* **107**.5 (2011): 056404.

[3] Matsuyama, K, and Gweon, G-H. Phenomenological Model for the Normal-State Angle-Resolved Photoemission Spectroscopy Line Shapes of High-Temperature Superconductors. *Physical Review letters* **111**.24 (2013): 246401.

[4] Hüfner, Stephan. Photoelectron spectroscopy: principles and applications. Springer Science and Business Media, 2013.

[5] L. Hedin and S. Lundqvist, in *Solid State Physics*, edited by F. Seitz, D. Turnbull, and H. Ehrenreich (Academic, New York, 1969), Vol. 23, p. 1.

[6] Bardyszewski, Witold, and Lars Hedin. A new approach to the theory of photoemission from solids. *Physica Scripta* **32**.4 (1985): 439.

[7] Varma, C. M., et al. Phenomenology of the normal state of Cu-O high-temperature superconductors. *Physical Review Letters* **63**.18 (1989): 1996.

[8] Anderson, Philip W. Hidden Fermi liquid: The secret of high-T c cuprates. *Physical Review B* **78**.17 (2008): 174505.

[9] Orgad, Dror, et al. Evidence of electron fractionalization from photoemission spectra in the high temperature superconductors. *Physical review letters* **86**.19 (2001): 4362.

[10] Meevasana, W., et al. Extracting the spectral function of the cuprates by a full two-dimensional analysis: Angle-resolved photoemission spectra of Bi 2 Sr 2 Cu O 6. *Physical Review B* **77**.10 (2008): 104506.

[11] Bansil, A., and M. Lindroos. Matrix element effects in the angle-resolved photoemission spectrum of BISCO. *Journal of Physics and Chemistry of Solids* **59**.10 (1998): 1879-1883.

[12] Kaminski, A., et al. Momentum anisotropy of the scattering rate in cuprate superconductors. *Physical review B* **71**.1 (2005): 014517.

[13] Valla, T., et al. "Evidence for quantum critical behavior in the optimally doped cuprate Bi2Sr2CaCu2O8+ ?." Science 285.5436 (1999): 2110-2113.

[14] Gweon, G-H., J. W. Allen, and J. D. Denlinger. Generalized spectral signatures of electron fractionalization in quasi-one-and two-dimensional molybdenum bronzes and superconducting cuprates. *Physical Review B* **68**.19 (2003): 195117.

[15] Shastry, B. Sriram. Extremely correlated Fermi liquids: The formalism. *Physical Review B* **87**.12 (2013): 125124.

[16] Hansen, Daniel, and B. Sriram Shastry. Extremely correlated Fermi liquids: Self-consistent solution of the second-order theory. *Physical Review B* **87**.24 (2013): 245101.

[17] Shastry, B. Sriram. Shastry Replies. *Physical Review Letters* **108**.2 (2012): 029702.

[18] Casey, Philip A., et al. Accurate theoretical fits to laser-excited photoemission spectra in the normal phase of high-temperature superconductors. *Nature Physics* **4**.3 (2008): 210-212.

[19] Yoshida, T., *et al.* Low-energy electronic structure of the high-Tc cuprates $La_{2-x}Sr_xCuO4$ studied by angle-resolved photoemission spectroscopy. *Journal of Physics: Condensed Matter* **19**.12 (2007): 125209.

[20] Markiewicz, R. S., et al. One-band tight-binding model parametrization of the high-T c cuprates including the effect of k z dispersion. *Physical Review B* **72**.5 (2005): 054519.

[21] Pavarini, E., et al. Band-structure trend in hole-doped cuprates and correlation with T c max. *Physical Review Letters* **87**.4 (2001): 047003.

[22] Gweon, G-H., et al. A spectroscopic fingerprint of electron correlation in high temperature superconductors. arXiv preprint arXiv:1310.4668 (2013).

[23] Žitko, R., *et al.* Extremely correlated Fermi liquid theory meets dynamical mean-field theory: Analytical insights into the doping-driven Mott transition. *Physical Review B* **88**.23 (2013): 235132.

[24] Perepelitsky, Edward, and B. Sriram Shastry. Extremely correlated Fermi liquids in the limit of infinite dimensions. *Annals of Physics* **338** (2013): 283-301.

[25] Shastry, B. Sriram. Anatomy of the self-energy. *Physical Review B* **84**.16 (2011): 165112.

[26] Kokalj, Jure, and Ross H. McKenzie. Consistent description of the metallic phase of overdoped cuprate superconductors as an anisotropic marginal Fermi liquid. *Physical review letters* **107**.14 (2011): 147001.

[27] Chang, Johan, et al. Anisotropic quasiparticle scattering rates in slightly underdoped to optimally doped high-temperature La 2? x Sr x CuO 4 superconductors. *Physical Review B* **78**.20 (2008): 205103.

[28] Zhou, X-J., *et al.* High-temperature superconductors: universal nodal Fermi velocity. *Nature* **423**.6938 (2003): 398-398.

[29] Johnson, P. D., *et al.* Doping and temperature dependence of the mass enhancement observed in the cuprate Bi2 Sr2 CaCu2 $O_{8+\delta}$. *Physical Review Letters* **87**.17 (2001): 177007.

[30] Lanzara, A., *et al.* Evidence for ubiquitous strong electronphonon coupling in high-temperature superconductors. *Nature* **412**.6846 (2001): 510-514.

[31] Kaminski, A., *et al.* Renormalization of spectral line shape and dispersion below Tc in Bi2 Sr2 CaCu2 $O_{8+\delta}$. *Physical Review Letters* **86**.6 (2001): 1070.

[32] Sato, T., *et al.* Observation of band renormalization effects in hole-doped high-T c superconductors. *Physical Review letters* **91**.15 (2003): 157003.

[33] He, J. *et. al.*, Coexistence of Two Sharp-Mode Couplings and their Unusual Momentum Dependence in the Superconducting State of Bi2 Sr2 CaCu2 $O_{8+\delta}$ Revealed by Laser-Based Angle-Resolved Photoemission. *Physical Review Letters* **111**.10 (2013): 107005.

[34] Shastry, B. Sriram. Theory of extreme correlations using canonical Fermions and path integrals. *Annals of Physics* **343** (2014): 164-199.DOI:http://dx.doi.org/10.1016/j.aop.2014.02.005. (Erratum) *Ann. Phys.* **373**, 717-718 (2016). DOI:http://dx.doi.org/10.1016/j.aop.2016.08.015.

[35] Shastry, B. Sriram, and Edward Perepelitsky. Low-energy physics of the t-J model in $d = \infty$ using extremely correlated Fermi liquid theory: Cutoff second-order equations. *Physical Review B* **94**.4 (2016): 045138.

[36] Garcia, D. R., and A. Lanzara. Through a Lattice Darkly: Shedding Light on Electron-Phonon Coupling in the High Tc Cuprates. *Advances in Condensed Matter Physics* 2010 (2010).

[37] Mishchenko, A. S., *et al.* Polaronic metal in lightly doped high-Tc cuprates. *EPL (Europhysics Letters)* **95**.5 (2011): 57007.

[38] McQueeney, R. J., *et al.* Anomalous dispersion of LO phonons in La1.85 Sr0.15 CuO4 at low temperatures. *Physical Review Letters* **82**.3 (1999): 628.

[39] Pintschovius, L., and M. Braden. Anomalous dispersion of LO phonons in La1.85 Sr0.15 CuO4. *Physical Review B* **60**.22 (1999): R15039.

[40] Fukuda, T., *et al.*Doping dependence of softening in the bond-stretching phonon mode of La_{2-x} Srx CuO4 ($0 \leq x \leq 0.29$).*Physical Review B* **71**.6 (2005): 060501.

[41] Vignolle, B., *et al.* Two energy scales in the spin excitations of the high-temperature superconductor $La_{2?x}$SrxCuO4. *Nature Physics* **3**.3 (2007): 163-167.

[42] Yang, K., *et al.* Normal-state electronic structure in the heavily overdoped regime of Bi1.74 Pb0.38 Sr1.88 Cu $O_{6+\delta}$ single-layer cuprate superconductors: An angle-resolved photoemission study. *Physical Review B* **73**.14 (2006): 144507.

[43] Meevasana, W., *et al.* Hierarchy of multiple many-body interaction scales in high-temperature superconductors. *Physical Review B* **75**.17 (2007): 174506.

[44] Graf, Jeff, *et al.* Bond stretching phonon softening and kinks in the angle-resolved photoemission spectra of optimally doped Bi2 Sr1.6 La0.4 Cu2 $O_{6+\delta}$ superconductors. *Physical Review Letters* **100**.22 (2008): 227002.

[45] Bogdanov, P. V., *et al.* Evidence for an energy scale for quasiparticle dispersion in Bi2 Sr2 CaCu2 O8. *Physical Review Letters* **85**.12 (2000): 2581.

[46] Vig, Sean, *et al.* Low-energy bosonic modes in a high-temperature superconductor with incipient charge order. arXiv preprint arXiv:1509.04230 (2015).

[47] Fong, H. F., *et al.* Neutron scattering from magnetic excitations in Bi2Sr2CaCu2O$_{8+\delta}$. *Nature* **398**.6728 (1999): 588-591.

[48] He, H., *et al.* Resonant spin excitation in an overdoped high temperature superconductor. *Physical Review Letters* **86**.8 (2001): 1610.

[49] Ideta, S., *et al.* Anisotropy of gap and kink energies in the trilayer high-Tc cuprate superconductor Bi2Sr2Ca2Cu3O$_{10+\delta}$. *Journal of Physics: Conference Series* **108**.1 (2008).

[50] Ideta, S., *et al.* Effect of electron-phonon coupling in the ARPES spectra of the trilayer cuprate Bi2Sr2Ca2Cu3O$_{10+\delta}$. *Journal of Physics: Conference Series* **428**.1 (2013).

[51] Borisenko, S. V., *et al.* Kinks, nodal bilayer splitting, and interband scattering in YBa2 Cu3 O$_{6+x}$. *Physical Review Letters* **96**.11 (2006): 117004.

[52] Reichardt, W., *et al.* Phonons in YBa2Cu3O$_{7-\delta}$. *Physica C: Superconductivity* **162** (1989): 464-465.

[53] Pintschovius, L., *et al.* Oxygen phonon branches in YBa2 Cu3 O7. *Physical Review B* **69**.21 (2004): 214506.

[54] Rossat-Mignod, J., *et al.* Neutron scattering study of the YBa2 Cu3 O$_{6+x}$ system. *Physica C: Superconductivity* **185** (1991): 86-92.

[55] Mook, H. A., *et al.* Polarized neutron determination of the magnetic excitations in YBa2 Cu3 O$_7$. *Physical Review Letters* **70**.22 (1993): 3490.

[56] Dai, P., *et al.* Magnetic Dynamics in Underdoped YBa2 Cu3 O_{7-x}: Direct Observation of a Superconducting Gap. *Physical Review Letters* **77**.27 (1996): 5425.

[57] Dai, Pengcheng, *et al.* Evolution of the resonance and incommensurate spin fluctuations in superconducting YBa2 Cu3 O_{6+x}. *Physical Review B* **63**.5 (2001): 054525.

[58] Vishik, I. M., *et al.* Angle-resolved photoemission spectroscopy study of Hg Ba2 $CuO_{4+\delta}$. *Physical Review B* **89**.19 (2014): 195141.

[59] dAstuto, Matteo, *et al.* Phonon dispersion in the one-layer cuprate $HgBa2CuO_{4+\delta}$. *Journal of Physics: Condensed Matter* **15**.50 (2003): 8827.

[60] Li, Yuan, *et al.* Hidden magnetic excitation in the pseudogap phase of a high-Tc superconductor. *Nature* **468**.7321 (2010): 283-285.

[61] Li, Yuan, *et al.* Two Ising-like magnetic excitations in a single-layer cuprate superconductor. *Nature Physics* **8**.5 (2012): 404-410.

[62] Chan, M. K., *et al.* Commensurate antiferromagnetic excitations as a signature of the pseudogap in the tetragonal high-Tc cuprate $HgBa2CuO_{4+\delta}$. *Nature communications* **7** (2016).

[63] Chen, Yulin, *et al.* Unusual layer-dependent charge distribution, collective mode coupling, and superconductivity in multilayer cuprate Ba2 Ca3 Cu4 O8 F2. *Physical Review Letters* **103**.3 (2009): 036403.

[64] Ronning, F., *et al.* Evolution of a metal to insulator transition in $Ca_{2-x}Na_x$ Cu

O2 Cl2 as seen by angle-resolved photoemission. *Physical Review B* **67**.16 (2003): 165101.

[65] Mannella, Norman, *et al.* Nodal quasiparticle in pseudogapped colossal magnetoresistive manganites.*Nature* **438**.7067 (2005): 474-478.

[66] Valla, T., *et al.* Charge-density-wave-induced modifications to the quasiparticle self-energy in 2H-TaSe 2. *Physical Review Letters* **85**.22 (2000): 4759.

[67] Brusdeylins, G., *et al.* He-atom scattering study of the temperature-dependent charge-density-wave surface structure and lattice dynamics of 2H-TaSe2 (001). *Physical Review B* **41**.9 (1990): 5707.

[68] Schafer, J., *et al.* Electronic quasiparticle renormalization on the spin wave energy scale. *Physical Review Letters* **92**.9 (2004): 097205.

[69] Brouet, V., *et al.* Measuring Fermi velocities with ARPES in narrow band systems: The case of layered cobaltates. *Journal of Electron Spectroscopy and Related Phenomena* **185**.5 (2012): 146-151.

[70] Cuk, T., *et al.* A review of electron-phonon coupling seen in the high-Tc superconductors by angle-resolved photoemission studies (ARPES). *Physica Status Solidi (b)* **242**, 1129 (2005).

[71] Migdal, A. B. Interaction between electrons and lattice vibrations in a normal metal. *Sov. Phys. JETP* **7**.6 (1958): 996-1001.

[72] Engelsberg, S. and J. R. Schrieffer. Coupled electron-phonon system. *Physical Review* **131**.3 (1963): 993.

[73] Gunnarsson, O., V. Meden, and K. Schnhammer. Corrections to Migdals theorem for spectral functions: A cumulant treatment of the time-dependent Greens function. *Physical Review B* **50**.15 (1994): 10462.

[74] Chubukov, A. V., and M. R. Norman. Dispersion anomalies in cuprate superconductors. *Physical Review B* **70**.17 (2004): 174505.

[75] Norman, M. R. Linear response theory and the universal nature of the magnetic excitation spectrum of the cuprates. *Physical Review B* **75**.18 (2007): 184514.

[76] Shastry, B. Sriram, Edward Perepelitsky, and Alex C. Hewson. Extremely correlated Fermi liquid study of the U= ∞ Anderson impurity model. *Physical Review B* **88**.20 (2013): 205108.